



1

2 **The high-resolution version of TM5-MP for optimised satellite retrievals: Description and Validation.**

3

4 **J. E. Williams¹, K. F. Boersma^{1,2}, P. Le Sager¹, W. W. Verstraeten^{1,2,*}**

5

6 [1] {KNMI, De Bilt, The Netherlands}

7 [2] {Meteorology and Air Quality Group, Wageningen University, Wageningen, The Netherlands}

8 [*] now at: KMI, Ukkel, Brussels, Belgium

9

10 **Abstract**

11 We provide a comprehensive description of the high-resolution version of the TM5-MP global Chemistry-
 12 Transport Model which is employed to provide highly resolved vertical profiles of nitrogen dioxide (NO₂),
 13 formaldehyde (CH₂O), and sulphur dioxide (SO₂) for use in satellite retrievals from platforms such as the Ozone
 14 Monitoring Instrument (OMI) and the Sentinel-5 Precursor, the TROPOspheric Monitoring Instrument
 15 (TROPOMI). Comparing seasonal differences in the global distributions of ²²²Rn we show that there are
 16 generally differences of ±20%, with larger increases occurring near specific coastal and decreases over specific
 17 tropical ocean regions. Analyzing vertical profiles of ²²²Rn above strong nitrogen oxide (NO_x) source regions,
 18 we show that there are differences in the strength of the convective activity of around ~2-10% (~10-20%) at 1° x
 19 1° constrained below 700hPa (200hPa) in the NH (tropics). We analyze the global distribution and chemical
 20 budget terms for tropospheric ozone (O₃), the reactive NO_x and N-reservoir species from simulations performed
 21 at 1° x 1° horizontal resolution. Compared to simulations at 3° x 2°, we show that although the impact on
 22 photolysis rates may be important regionally, changes in the seasonal means representative of the boundary layer
 23 are of the order of a few percent, in spite of the higher spatial variability of meteorological data fields from
 24 ERA-Interim. Surface concentrations of O₃ in high-NO_x regions decrease by between ~5-10% at 1° x 1° as a
 25 result of a reduction in NO_x recycling terms and an increase in the titration term of O₃ involving NO. At 1° x 1°
 26 the net global stratosphere-troposphere exchange of ozone decreases by ~7%, dominated by substantial
 27 reductions in the Northern Hemisphere somewhat offset by increases in down-welling which occurs in the
 28 Southern Hemisphere. By comparing NO, NO₂, HNO₃ and PAN profiles against a host of measurements made
 29 across large regional domains, we show that TM5-MP captures the vertical distribution of NO_x and long-lived
 30 NO_x reservoirs at background locations, but exhibits a too high NO/NO₂ ratio in the Free Troposphere, with
 31 changes at 1° x 1° being limited to a few percent. Surface mixing ratios in both NO and NO₂ are generally under-
 32 estimated in both low and high NO_x scenarios. For Europe, we show that there is a negative bias in NO
 33 concentrations at the surface across the whole domain, with lower biases at 1° x 1° at only ~20% of sites. For
 34 NO₂, biases are more variable, with lower (higher) biases occurring at ~35% (~20%) of sites. For nitric acid
 35 (HNO₃) there is a seasonal cycle present at the surface in TM5-MP which is not observed, leading to a low bias
 36 during wintertime and a high bias during summertime. For the shorter-lived NO_x reservoirs, no significant
 37 changes occur with the exception of N₂O₅ due to ~10% perturbations in the NO₃ radical. For CH₂O, the impact
 38 of higher resolution on the chemical budget terms is rather modest, with changes less than 5%. The simulated
 39 vertical distribution of CH₂O agrees reasonably well with measurements in pristine locations, but CH₂O vertical
 40 column densities are generally underestimated relative to satellite measurements in polluted regions. For SO₂,
 41 the performance at 1° x 1° is principally governed by the quality of the emission inventory, with limited



improvements in the site specific biases with most showing no significant improvement. For the vertical column, improvements near strong source regions occur which reduce the biases in the integrated column.

44

1. Introduction

46

One application of Chemistry Transport Models (CTM) is to provide accurate vertical and horizontal global distributions of trace gases such as ozone (O_3), nitrogen dioxide (NO_2), sulphur dioxide (SO_2) and formaldehyde (CH_2O) that are used as *a-priori* best-guesses in the retrievals of tropospheric abundances from earth-orbiting satellites including the Tropospheric Emission Sounder (TES, Worden et al., 2007) Global Ozone Monitoring Experiment (GOME), SCanning Imaging Absorption spectroMeter for Atmospheric CHartographY (SCIAMACHY, De Smedt et al., 2008), the Ozone Monitoring Instrument (OMI, Boersma et al., 2011), and GOME-2 (Valks et al., 2011)). To date, although high-resolution regional models have been employed for selected regions such as the US and Europe (e.g. Russell et al., 2011; Zhou et al., 2012; Vinken et al., 2014), at global scale the CTMs resolutions employed are still rather coarse (between 2-4° latitude and 2-6° longitude), resulting in ‘footprints’ of hundreds of kilometers in area. This has limitations as the resulting total columns are sensitive to topography, surface albedo and the shape of the *a-priori* vertical profiles themselves. This sampling is rather coarse and leads to substantial errors in the retrievals (e.g. Boersma et al., 2007; Heckel et al., 2011; Russell et al., 2011) and imposes constraints on capturing the regional scale variability in short-lived trace gas abundances observed from high-resolution satellite instruments such as OMI.

This lack of spatial detail is particularly relevant for situations where strong spatio-temporal variability in the vertical distribution of NO_2 , SO_2 , and CH_2O can be expected. Examples include shipping lanes in the relatively unpolluted Marine Boundary Layer (e.g. Vinken et al., 2014) and coal-fired power plant SO_2 pollution (e.g. Fioletov et al., 2015). Moreover, during the day the local lifetime and mixing ratios of trace gases such as NO_2 are critically dependent on a host of variables e.g. temperature, surface albedo, cloud cover (via photolysis), chemical conversion (i.e. NO/NO_2 ratio) and the extent of mixing by convective upwelling (i.e. land type) and advective transport. Thus, the information provided for the retrievals are all affected by the coarsening procedure that is necessary in the CTM. Recently, Heckel et al. (2011) demonstrated that there is an associated uncertainty of ~2 using *a-priori* data from a global CTM rather than a regional CTM, principally due to loss of spatial information. Two other studies focusing on the impact of horizontal resolution on the retrieval of vertical column densities (VCD) of NO_2 suggested that errors of up to ~50% exist (Yamaji et al., 2014; Lin et al., 2014). This problem becomes accentuated for the next generation of earth orbiting satellites such as the Tropospheric Monitoring Instrument (tropOMI), which has a smaller footprint compared to its predecessors (Veefkind et al., 2012). Applications of TM5 include the retrieval of NO_2 , CH_2O , and SO_2 column densities from OMI and tropOMI (e.g. van Geffen et al., 2016), where studies related to the influence of horizontal resolution have been limited principally to NO_2 .

The dominant tropospheric loss terms for CH_2O are photolysis and scavenging into cloud droplets (wet deposition; Jacob, 2000). Thus the atmospheric lifetime of CH_2O is highly sensitive to the extent of cloud cover and the vertical profiles of the photolysis rates. A dominant application of CH_2O retrievals is for placing constraints in tropical and sub-tropical isoprene emission fluxes (e.g. Palmer et al., 2006; Stavrakou et al., 2009; Marais et al., 2012). The resulting emission estimates are highly sensitive to the stoichiometric yield of CH_2O



from isoprene oxidation, the chemical lifetime of CH_2O and spatial differences in land cover. Other applications include estimating yields released during Biomass Burning (BB) episodes (Gonzi et al., 2011), whose spatial location is also smeared via the coarsening procedure. For SO_2 , which predominantly originates from point sources, an adequate spatial distribution of such sources is crucial for deriving accurate biases in existing emission inventories.

In this paper we provide a comprehensive description of the global, high-resolution $1^\circ \times 1^\circ$ version of the TM5 CTM tailored for the application of satellite retrievals (hereafter referred to as TM5-MP). In Sect. 2 we give details related to the modifications which have been made to the TM5 model compared to previous versions, the emission inventories employed, updates that have been made to the modified CB05 chemical mechanism, stratospheric boundary conditions, photolysis scheme, heterogeneous conversion and model structure. In Sect. 3 we analyse the impact on convective and advective transport of trace species from the boundary layer as derived using Radon distributions. In Sect. 4 we investigate the effects on regional photolysis frequencies and in Sect. 5 we examine the differences introduced for both tropospheric O_3 , NO_x and N-containing species at higher resolution and make comparisons against both surface and aircraft measurements to investigate effects. In Sect 6 we examine impact on the global CH_2O budget and integrated columns, and in Sect. 7 we show the subsequent improvement in the distribution of SO_2 at $1^\circ \times 1^\circ$. In Sect. 8, we present our conclusions.

98

99 **2 Description of TM5-MP**

100

Previous versions of TM5 (TM5-chem-v3.0, Huijnen et al., 2010) included a two-way nested zooming option as described by Krol et al. (2005). This option allowed high-resolution simulations to be performed over any pre-defined regional, with boundary conditions being determined by the global simulation at coarser resolution. Typically, global simulations at $3^\circ \times 2^\circ$ with zoom regions at $1^\circ \times 1^\circ$ were performed to alleviate the long runtime of a global $1^\circ \times 1^\circ$ run. In the new version of TM5 (hereafter referred to as TM5-MP; the massivelyintersta parallel version), the usage of MPI has been totally rewritten. Zoom regions are no longer available, but data sets are distributed along longitudes and latitudes, instead of model levels and tracers. The advantages of that overhaul towards domain decomposition are a smaller memory requirement and the possibility to use more processors making global $1^\circ \times 1^\circ$ simulations feasible in terms of runtime and affordable in terms of computing resources. A TM5-MP global $3^\circ \times 2^\circ$ ($1^\circ \times 1^\circ$) run is ~ 6 (~ 20) times faster than the previous version of TM5 (Huijnen et al., 2010) for similar resources.

Here we provide a comprehensive description of the modifications and updates introduced into TM5-MP compared to TM5 v3.0 (Huijnen et al., 2010). The model is driven using the ERA-interim meteorological re-analysis (Dee et al., 2011) and updated every 3 hours, with interpolation of fields for the intermediate time periods. The convective mass fluxes are taken from ERA-interim dataset and describe the updraft velocities from the boundary layer into the free troposphere (FT), which replaces the parameterization of Tiedtke (1989). An iterative time-step is employed to prevent too much mass being transported out of any particular grid cell for any particular time-step according to the Courant-Friedrichs-Lewy (CFL) criteria (Bregman et al., 2003), which is especially relevant when reducing the size of grid-cells as done here.



The gas phase chemistry in TM5-MP is described by an expanded version of the modified CB05 chemical mechanism (hereafter mCB05; Williams et al., 2013). We have placed emphasis of updating and expanding the fast NO_x chemistry to account for an accurate partitioning of nitrogen for higher NO_x regimes than those occurring at coarser horizontal resolutions. All reaction rate data is now taken from the latest IUPAC recommendations (sited at <http://iupac.pole-ether.fr/>; last access June 2016) using updated formulations for third-body collisions, where the rate data for fast NO_x and CH_2O chemistry is given in Table 1. This includes the recent update to the formation rate of HNO_3 determined by Möllner et al. (2010). The most relevant modifications are: (i) The yield of CH_2O , methanol (CH_3OH) and the hydro-peroxy radical (HO_2) from the self-termination of the methyl-peroxy radical (CH_3O_2) is increased according to Yarwood et al. (2005), (ii) the direct formation of CH_2O from the reaction of $\text{CH}_3\text{O}_2 + \text{HO}_2$ is added using the temperature dependent branching ratio defined in Atkinson et al. (2004), (iii) the production of HNO_3 during the oxidation of di-methyl sulphide (DMS) by the NO_3 is now included, (iv) explicit organic peroxy radicals have been introduced as products from the oxidation of propene (C_3H_6) and propane (C_3H_8) by OH, which are lost by either the reaction with nitric oxide (NO) or HO_2 allowing the in-situ chemical formation of acetone (CH_3COCH_3) and higher aldehydes (ALD2), respectively, following the stoichiometry given in Emmons et al. (2010), (v) a second product channel for N_2O_5 photolysis is added producing NO, (vi) the formation and photo-dissociation of HONO has been included, (vii) the formation and transport of methyl peroxy nitrate ($\text{CH}_3\text{O}_2\text{NO}_2$) is also included (Browne et al., 2011), and (viii) modifications to the gas-phase chemistry involving NH_3 have been introduced following the stoichiometry given in Hauglestaïne et al. (2014). This version of the modified CB05 chemical mechanism is hereafter referred to as mCB05v2.

The calculation of height resolved photolysis rates (J values) is performed using a tailored version of the Modified Band Approach (MBA). The implementation and performance of this parameterization in TM5 has been fully described in Williams et al. (2012). For the calculation of the height-resolved Actinic Fluxes at the seven specific wavelengths used for calculating the J values (these being 205.1nm, 287.9nm, 302.0nm, 311.0nm, 326.5nm, 385.0nm and 610.0nm), the 2-stream radiative transfer solver of Zdunkowski et al. (1980) is embedded into TM5-MP. Details regarding the parameterizations used to account for the scattering and absorption introduced by gaseous molecules, aerosols and clouds the reader is referred to Williams et al. (2012). For aerosols, the climatology of Shettle and Fenn (1979) is included. The calculation of the effective radius (r_{eff}) of cloud droplets is now performed using the approach of Martin et al. (1994), where different parameter values are used for over the land and ocean using cloud condensation nuclei concentrations of 40 and 900, respectively. Due to potentially erroneous values at low horizontal resolution, we weight the final r_{eff} value using the land fraction in each grid-cell. We apply limits between 4-16 μm on the resulting r_{eff} values. This improves the representation of the scattering component due to cloud droplets used for the calculation of the actinic flux in the lower troposphere (not shown). For the scattering effects from cloud droplets, we subsequently downsize the physical r_{eff} by $\sim 0.5\text{-}2\mu\text{m}$ to account for the relationship between the optical and physical r_{eff} values.

For aerosols, an aerosol scheme is available for use within TM5-MP (aan den Brugh et al., 2010), but we choose not to use it for the purpose of satellite retrievals due to the extra computational expense needed when performing high resolution simulations that would potentially hinder operational use. We acknowledge that the description of aerosols in this study is rather crude and increasing scattering could have an impact under instances of low cloud coverage. For the application of TM5-MP towards satellite retrieval, it is preferable to use



any advancements in computational performance on further increases in the horizontal resolution employed. Therefore it is not currently envisaged that a full description of aerosol processes will be included during operational satellite retrievals.

However, heterogeneous conversion processes still need the description of the total reactive Surface Area Density (SAD) from aerosols. In TM5-MP this is assumed as the cumulative value of contributions from sulphate, nitrate, ammonium and methane sulphonic acid as calculated by the EQUilibrium Simplified Aerosol Model (EQSAM) approach (Metzer et al., 2002), thus the secondary organic aerosol component is not included. The distribution of these aerosol species is calculated online and coupled to the respective gaseous precursors. The density of each aerosol type (1.7 g/cm^3) and r_{eff} (of between $0.18\text{-}0.2\mu\text{m}$) is prescribed as in Huijnen et al. (2014). Swelling at higher relative humidities ($> 70\%$) is crudely accounted for by increasing r_{eff} to between $0.25\text{-}0.27\mu\text{m}$. The contributions due to sea-salt, black carbon and organic carbon towards heterogeneous loss are not accounted for. Temperature dependent gas phase diffusion co-efficients (D_g) are used in the derivation of the pseudo first-order heterogeneous rate constants based on the theory of Schwartz (1986).

For N_2O_5 , the uptake coefficient (γ) is calculated using the parameterization of Evans and Jacob (2005), therefore dependent on both temperature and relative humidity. Once a surface reaction with H_2O occurs two molecules of nitric acid (HNO_3) are formed. No uptake on cirrus particles is included for HNO_3 , which can lead to de-nitrification of the upper troposphere (Lawrence and Crutzen, 1998; von Kuhlmann and Lawrence, 2006). For HO_2 we adopt a fixed $\gamma_{\text{HO}_2} = 0.06$ across all aerosol types as taken from Abbatt et al. (2012) and for NO_3 we adopt a fixed $\gamma_{\text{NO}_3} = 10^{-3}$ as recommended by Jacob (2000). For HO_2 , heterogeneous conversion forms 0.5 molecules of Hydrogen Peroxide (H_2O_2), whereas for NO_3 it forms one molecule of HNO_3 is formed, following Emmons et al. (2010). For the SAD associated with cloud droplets we use the r_{eff} values that are calculated by Martin et al. (1994) thus maintaining consistency between the size of the cloud droplets used for the scattering component in the calculation of J values and heterogeneous loss rates on the clouds. By using the ECMWF cloud fraction for each respective grid cell, we assume that instantaneous mixing throughout the grid cell does not occur in order to avoid exaggerated conversion rates on cloud surfaces.

As TM5-MP contains no explicit stratospheric chemistry, we apply constraints above the tropopause to ensure realistic Stratosphere-Troposphere Exchange (STE) of O_3 and for constraining the incoming radiation reaching the troposphere needed for the MBA (Williams et al., 2012). For stratospheric O_3 , we use total column values derived from the assimilation of satellite observations as provided in the improved version of the Multi-Sensor Re-analysis (MSR, van der A., 2010), which is vertically distributed according to the climatology of Fortuin and Kelder (1998). Three distinct zonal bands are used for nudging the stratospheric O_3 fields, these being 30°S - 30°N , $30\text{-}66^\circ\text{S/N}$ and $> 66^\circ\text{S/N}$, where nudging occurs at pressure levels $<45\text{hPa}$, $<95\text{hPa}$ and $<120\text{hPa}$, with relaxation times of 2.5 days, 3 days and 4 days, respectively.

For stratospheric CH_4 we use the monthly 2D climatological fields provided by Grooß and Russell (2005), with the nudging heights and relaxation times being identical to those used for stratospheric O_3 . For stratospheric CO and HNO_3 we constrain mixing ratios by using monthly mean ratios between CO/O_3 (Dupuy et al., 2004) and HNO_3/O_3 (Jégou et al., 2008; Urban et al., 2009) based on the latitudinal climatologies derived from ODIN observations between 2003/2004 and 2001-2009. In order to avoid jumps in the nudging constraints between months, we gradually change between ratios using the total monthly difference/number of days in the month.



These ratios are applied using the monthly mean stratospheric O_3 distribution in TM5-MP, which is constrained by the MSR dataset (van der A et al., 2010). For both species, model fields are nudged at 5.5hPa, 10hPa and 28hPa using relaxation times of 5, 10 and 60 days, respectively. Previous versions of TM5 used a HNO_3 climatology from the UARS MLS instrument and applied nudging constraints at 10hPa only (Huijnen et al., 2010).

204

2.2 Emission inventories

All emission inventories applied in TM5-MP are yearly specific meaning that the year-to-year variability in emission fluxes due to changes in anthropogenic activity, biogenic activity and burning extent are taken into account. For the anthropogenic emission of NO_x , CO , SO_2 , NH_3 and Non-Methane Hydrocarbons (NMVOC) we adopt the MACCity emission estimates described in Granier et al. (2011). The lack of sector-specific information complicates the use of daily cycles for e.g. the road transport component. For volcanic SO_2 emissions, the estimated emission flux has been scaled up to 10 Tg S/year based on Halmer et al. (2002). For the biogenic component, where available we use the CLM-MEGANv2.1 emission inventories produced for the Southern Hemispheric Multi-model Intercomparison Project (SHMIP) as described in Zeng et al. (2015), with the missing trace species (e.g. ethane, propane, higher organics) coming from alternative MEGAN simulations as outlined in Sindelarova et al. (2014). A diurnal cycle is imposed on the isoprene emissions and introduced into the first ~50m between 20°S-20°N. The BB emissions are taken from the monthly estimates provided by the GFEDv3 inventory (van der Werf et al., 2010) and latitude dependent injection heights and a tropical burning cycle are implemented following Huijnen et al. (2010). All emission inventories are provided on a 0.5° x 0.5° resolution and subsequently coarsened onto the horizontal resolution used during any particular simulation. For lightning NO_x we use the parameterization which uses convective precipitation of Meijer et al. (2001) and constrain to a total global emission of ~6Tg/N yr⁻¹. This uses the convective flux values meaning that re-scaling of the nudging term was necessary in order to achieve similar total lightning NO_x across simulations. In TM5-MP all NO_x emissions are introduced as NO , rather than speciating a fraction which is emitted directly as NO_2 (Carslaw and Beevers, 2005). Global NO_x emissions for the year 2006 total 49 Tg N yr⁻¹ (including lightning). Other notable species include CO (1081 Tg CO yr⁻¹), SO_2 (117 Tg S yr⁻¹), CH_2O (13.5 Tg C yr⁻¹) and isoprene (510 Tg C yr⁻¹). An overview of the global and zonal emissions terms used in the simulations analysed here are given in Table 3.

Latitudinal constraints on CH_4 global distributions are applied using the methodology outlined in Banda et al. (2015). We also introduce similar constraints based on the appropriate surface measurements for H_2 in order to account for the latitudinal gradient and variability across seasons, which replaces the fixed global value of 550ppb used in previous versions. Finally, for Radon (Rn^{222}) emissions we apply the estimates of Schery (2004).

2.3 Observations

Although the performance of mCB05 in TM5 v3.0 has been validated for selected Volatile Organic Compounds (VOC), O_3 , CH_2O , CO and NO_y in both hemispheres (Williams et al., 2013; 2014; Fisher et al., 2015; Zeng et al., 2015), the significant changes made to both the chemical scheme and the rate parameters in mCB05v2 necessitate independent validation at both 3° x 2° and 1° x 1°. We choose a range of ground-based and airborne



measurements taken at diverse locations representing a diverse range of chemical regimes. Here we briefly describe the observations utilised for this purpose.

For validation of simulated surface concentrations we use measurements of gaseous O_3 , NO, NO_2 , HNO_3 and SO_2 available from the European Monitoring and Evaluation program (EMEP, www.emep.int), where we exploit measurements taken at various background sites in Norway, Finland, The Netherlands, Belgium, Poland, Germany, Spain, Italy and Portugal. For the model composites we extract data from 3 hourly instantaneous output in order to assemble both the weekly and monthly mean values from the simulations. For the weekly comparisons of NO_2 and SO_2 we use values extracted at 13:00 local time, close to the overpass time of the OMI instrument (e.g. Boersma et al, 2008). The selected stations allow validation of the seasonality for both rural regions (FI37) and urban regions (NL09), where we include identical stations where possible for both species. For HNO_3 we assemble the weekly values from the daily averages.

Measured O_3 surface concentrations in the EMEP network are obtained using UV monitors (Aas et al. 2001). For all species, spatial interpolation of model data is performed accounting for the height of the measurement station and by weighting using the distance of the station from the surrounding grid cells. The wide range of measurement sites chosen insures that both background and polluted cases are assessed.

For validating the vertical distribution of relevant trace species such as O_3 , SO_2 and CH_2O , we use measurements by the DC-8 aircraft during the Intercontinental Chemical Transport Experiment B (INTEX-B; Singh et al., 2009) that took place between March and May 2006. Observations of a host of co-located nitrogen-containing species are available (namely NO, NO_2 , PAN and HNO_3). These flights were conducted over a wide region, and we use all three months of measurements. Each month sampled a different region representing different meteorological conditions and local emission sources, namely: the Gulf of Mexico (90-100°W, 15-30°N), the remote Pacific (176-140°W, 20-45°N) and around Alaska (160-135°W, 20-60°N) with flights to the south and west. Measurements cover altitudes up to 10.5km, and bin the values with respect to pressure using 50 hPa bins or less in the LT. We interpolated three-hourly output against measurements for each respective day, similar to the comparisons performed in previous evaluations of TM5 (e.g. Huijnen et al., 2010), but we segregate our comparisons into the three distinct regions. For details relating to the location of each flight the reader is referred to the campaign overview of Singh et al. (2009).

For tropospheric O_3 , we supplement the INTEX-B comparisons with those taken over more polluted regions as part of the Measurement of Ozone, water vapour, carbon monoxide and nitrogen oxides by Airbus In-service aircraft (MOZAIC; Thouret et al., 1998). We aggregate the measurements as seasonal means for December-January-February (DJF) and June-July-August (JJA) in order to provide a robust number of samples for each location. Here we chose to use profiles representative of the Northern mid-latitudes, namely: London (0.2°W, 51.2°N), Vienna (16.5°E, 48.1°N), Washington (77.5°W, 38.9°N), Portland (122.6°W, 45.6°N), Shanghai (121.8°E, 31.2°N) and Tokyo (140.4°E, 35.8°N).

We also make comparisons of O_3 , NO, NO_2 , selected N reservoir species, SO_2 and CH_2O profiles using measurements made aboard the NOAA WP-3D aircraft as part of the Second Texas Air Quality Study (TexAQS II; Parrish et al, 2009), which was conducted over the Texas sea-board during September and October 2006. This allows the assessment of TM5-MP over a region with higher VOC emissions and industrial activity. These measurements were typically sampled at altitudes below 500 hPa, therefore no UTLS measurements are available from this campaign.



3 The Effect on Atmospheric Transport

Here we analyse the differences in convective transport out of the boundary layer by analysing the vertical and horizontal distribution of ^{222}Rn , which is a diagnostic typically used for assessing the differences in transport in CTMs (e.g. Jacob et al., 1997). ^{222}Rn is emitted at a steady rate and exhibits a half-life of ~ 3.8 days, which is long enough to be transported from the boundary layer into the FT due to chemical passivity, with loss via wet scavenging and deposition being negligible. Therefore, it acts as an ideal tracer to assess differences in convective transport from the surface out of the boundary layer (BL).

Figure 1 shows seasonal mean horizontal global distributions of ^{222}Rn for DJF and JJA in the $1^\circ \times 1^\circ$ simulation averaged between 800-900hPa (i.e.) at the top of the BL including the lower FT highlighting the spatial variability in convective upwelling near the top of the convective boundary layer. Also shown are the associated percentage differences against the re-binned $3^\circ \times 2^\circ$ ^{222}Rn distribution, allowing a direct comparison. Resolution dependent differences result from the cumulative effects of the use of higher resolution mass fluxes from the ERA-interim meteorological data for describing convective activity and the more accurate temporal distribution of regional ^{222}Rn emissions at $1^\circ \times 1^\circ$. In general it can be seen that seasonal differences of $\pm 20\%$ exist, typically with increases over continents and decreases over oceans. Maximal differences of $>60\%$ occur near selected coasted regions (California, West Africa, Madagascar) or in outflow regions such as off South America and Africa, where differences exhibit a strong seasonal dependency. This is due to the large differences in convective strength due to the variability in heating rates, and thus temperatures, between land and ocean (e.g. Sutton et al., 2007).

A comparison of the ratio of the monthly mean ^{222}Rn profiles ($1^\circ \times 1^\circ / 3^\circ \times 2^\circ$) extracted above selected European cities for January (black) and July (blue) 2006 are shown in Figure S1 in the supplementary material. The typical tropospheric profile of ^{222}Rn exhibits an exponential decay from the LT to the FT (not shown). In order to homogenise the emission flux in the comparison, we coarsen the $1^\circ \times 1^\circ$ data onto the $3^\circ \times 2^\circ$ grid by averaging the six individual values into a representative mean column. The extent of the changes in the vertical distribution of ^{222}Rn is somewhat site specific meaning an in depth analysis is beyond the scope of this paper. In summary, the $1^\circ \times 1^\circ$ simulation generally provides stronger convective activity for January, with the main impact occurring below 700hPa (e.g. London and Paris). The changes in ^{222}Rn in the lower troposphere range between ~ 2 -10% (i.e. ratios of 0.9-1.1), implying both weaker and stronger convective transport depending on changes in location (i.e.) orography and land type. In that the impact at Berlin is larger than at e.g. Barcelona also shows that, surprisingly, the inclusion of a large ocean fraction (with weaker convective mixing) in the $3^\circ \times 2^\circ$ cell does not seem to introduce dominating effects. For July the changes in the vertical distribution extend into the FT up to 500hPa, although changes in the upper FT have a significant component due to changes in long-range transport. The magnitude of the changes are similar to those exhibited during January, although maybe of the opposite sign (e.g. Rome). Thus the influence on e.g. NO_2 , CH_2O and SO_2 *a-priori* vertical profiles will be non-negligible and diverse.

For the tropical cities located in regions where convective mixing is stronger, the corresponding differences can reach $\pm 20\%$, especially near the surface (e.g. Caracas and Karachi). There is a site-specific seasonal dependency in the magnitude of the changes related to the regional land characteristics (e.g. Lagos versus Kuala Lumpur).



Thus, potential differences in *a-priori* vertical profiles can be considerable compared to those provided at a $3^\circ \times 2^\circ$ resolution.

We also show comparisons of profiles from $1^\circ \times 1^\circ$ simulations using the convective scheme of Tiedke (1989) against those using the convective mass-fluxes from the ERA-interim meteorological dataset for Europe (Figure S3). For this comparison no averaging is employed, where the selected grid cells are near the centre of each urban conurbation. The residuals show that the significant differences exist, with the convective mass-fluxes from ERA-interim being somewhat weaker than those calculated online using Tiedke (1989) (i.e. the residual is typically less than 1, especially during July).

4 The Impact on tropospheric photolysis frequencies

The changes in the spatio-temporal distribution of cloud cover and surface albedo has the potential to alter the penetration depth and upwelling of photolysing light, and thus photochemical production and destruction terms. The similarity in the monthly mean photolysis frequencies for O_3 and NO_2 across resolutions (hereafter denoted J_{O_3} and J_{NO_2} , respectively) are shown in Figure S4 of the supplementary material. Comparisons of the monthly mean J_{O_3} and J_{NO_2} values are shown at five different locations identical to those shown in Williams et al. (2012). For J_{O_3} the impact of increasing resolution is limited to a few percent in the monthly mean values. At global scale this leads to a reduction of ~2% in the total mass of O_3 photolysed (not shown). For J_{NO_2} , the corresponding differences become more appreciable, with $1^\circ \times 1^\circ$ exhibiting ~5-10% higher values at high Northern latitudes (associated with the high- NO_x scenario).

Focusing on J_{NO_2} and comparing seasonal mean values near the surface shows that very similar spatial patterns occur for both simulations at global scale (c.f. Figure S5). The highest J_{NO_2} values occur over the tropical oceans and high altitude regions (e.g. Nepal). Although more regional fine-structure can be seen at $1^\circ \times 1^\circ$ (e.g. South-Western US for DJF and around Iceland for JJA), these seasonal averages show that the small perturbations shown in Fig. S3 extend to the global scale leading to a reduction of ~5% at $1^\circ \times 1^\circ$.

Comparisons of monthly mean profiles of J_{O_3} and J_{NO_2} extracted over the location of selected tropical cities are shown in the Figs. S6a and b, respectively, in the Supplementary Material. Here no averaging is performed towards an identical horizontal resolution, therefore values are representative of the J values directly above the selected urban centres. The J_{O_3} profiles are affected to a larger extent than the J_{NO_2} profiles due to the characteristic absorption spectra of each species, which makes J_{O_3} more sensitive to the additional scattering introduced due to clouds. Profiles over Dubai act as a proxy for clear-sky conditions, where values of unity exist in the residual of J_{O_3} and J_{NO_2} calculated through most of the column. The small difference at the surface is due to changes in the surface albedo between resolutions, with Dubai being situated on the coast meaning that a sharp horizontal gradient exists in surface albedo. For other cities, the largest perturbations occur away from the surface (e.g. Jakarta, Nairobi and Lagos) around the altitude where tropospheric clouds are most abundant. There are typically changes of between ± 5 -10% in the monthly mean profiles. The changes in J_{NO_2} reflect those simulated for J_{O_3} , with somewhat smaller perturbations.

5 Implications for oxidative capacity and tropospheric O_3



358 The partitioning of reactive N between the short- and long-lived chemical N-reservoirs included in TM5-MP
 359 depends on the oxidative capacity simulated for the troposphere via competition between the various different
 360 radicals i.e. OH, $\text{CH}_3\text{C}(\text{O})\text{O}_2$, NO_3 and CH_3O_2 . Therefore, changes to the distribution and resident mixing ratios
 361 of tropospheric O_3 subsequently impose changes on the fractional composition of the NO_y budget (e.g. Olszyna
 362 et al., 1994) and the also the efficiency of the NO_x re-cycling terms by altering the chain length (Lelieveld et al.,
 363 2004). In this section we analyse the global and zonal chemical budget terms for tropospheric O_3 to highlight the
 364 inter-hemispheric differences which occur (i.e.) under low and high- NO_x environments.
 365 Table 4 provides the zonally segregated chemical budget terms for tropospheric O_3 , from which the global
 366 component due to STE can be determined by closing the budget terms following the methodology given in
 367 Stevenson et al. (2006). The chemical tropopause calculated for $3^\circ \times 2^\circ$ is applied for the analysis of $1^\circ \times 1^\circ$
 368 budget terms to ensure that a valid comparison is performed, i.e. the same mass of air is accounted for. For
 369 computational efficiency the budget terms are aggregated in 10° latitudinal bins and summed across all
 370 longitudes providing the cumulative terms.
 371 The most significant change with resolution concerns STE. By using a dedicated tagged stratospheric O_3 tracer
 372 (which only undergoes photo-chemical destruction and deposition in the troposphere; O_3S) changes in the zonal
 373 STE can be determined. The stratospheric burden of O_3 (BO_3S) exhibits a strong hemispheric gradient with
 374 much more down-welling occurring in the NH peaking during boreal springtime. At global scale the STE
 375 exchange is $579 \text{ TgO}_3 \text{ yr}^{-1}$, which agrees well with the multi-model STE mean of $556 \pm 154 \text{ TgO}_3 \text{ yr}^{-1}$ in
 376 Stevenson et al. (2006), with observational estimates being $\sim 550 \pm 140 \text{ TgO}_3 \text{ yr}^{-1}$ (Olsen et al., 2001). This $\sim 7\%$
 377 reduction of STE at $1^\circ \times 1^\circ$ is encouraging considering that previous studies using TM5 have concluded that STE
 378 in TM5 at $3^\circ \times 2^\circ$ was biased high compared to STE inferred from TES and MLS satellite observations
 379 (Verstraeten et al. (2015)). The increase in STE in the SH, with an associated decrease in the NH (see below),
 380 implies that there is a shift in circulation patterns at $1^\circ \times 1^\circ$ even though the stratospheric BO_3 remains essentially
 381 unchanged. Previous studies have shown that in order to resolve the correct spatial and temporal stratosphere-
 382 troposphere flux, high resolution is required both in the horizontal and the vertical (e.g. Meloen et al., 2002).
 383 The NH STE diagnosed with TM5-MP is an order of magnitude smaller than estimates derived in a recent study
 384 also conducted at a $1^\circ \times 1^\circ$ resolution (Tang et al, 2011; $\sim 200 \text{ TgO}_3 \text{ yr}^{-1}$), which identified deep convection as
 385 important for STE. Here we use a different vertical grid and meteorological dataset to drive TM5-MP, both of
 386 which affect the ability towards capturing an accurate STE flux (Meloen et al., 2002).
 387 The zonal seasonal means of the fraction of O_3S to O_3 ($\text{O}_3\text{S}/\text{O}_3$) for both simulations are shown in Figure 2 for
 388 DJF and JJA. There is a clear seasonal zonal shift in the fractional contribution due to the O_3 transported
 389 downwards from the Stratosphere exhibiting a longer lifetime in the winter hemisphere reflecting a lower
 390 photochemical destruction rate. At $1^\circ \times 1^\circ$ the largest increase in STE occurs in the SH during JJA. Here $\sim 20\text{--}$
 391 25% of tropospheric O_3 is transported down from the stratosphere. Comparing the 0.2 contour for the NH mid-
 392 troposphere shows significant changes, extending further down towards the surface during boreal wintertime
 393 leading to the higher total mass of O_3S in the troposphere. The extent of nudging towards the MSR climatology
 394 is essentially constant across simulations (c.f. Table 4). Interestingly, less O_3S reaches the surface in the tropics
 395 at $1^\circ \times 1^\circ$ due to the enhanced chemical destruction term in the Free Troposphere. Approximately 10% of the
 396 global deposition term for O_3 is associated with O_3 that originates from the Stratospheric at $1^\circ \times 1^\circ$ (c.f. $\sim 5\%$ at
 397 $3^\circ \times 2^\circ$). For the NH, this contributes to the simulated increase in deposition of $\sim 9\%$.



For tropospheric O_3 there are similarities that occur between the NH, tropics and SH (i.e.) high and low- NO_x scenarios, resulting in a cumulative decrease in O_3 production of ~2-4% across zones. For the chemical loss terms there is a decrease of ~3% (~1%) in the NH (SH) reflective of the changes discussed for J_{O_3} , which acts as the primary destruction term. There is a zonal gradient in the tropospheric BO_3 following the zonal gradient in NO_x emissions. Comparing terms shows that BO_3 decreases at $1^\circ \times 1^\circ$ by a few percent at global scale (~7 Tg O_3) making a rather small impact on oxidative capacity. This is of the same order of magnitude as that found in previous studies concerned with horizontal resolution (e.g. Wild and Prather, 2006). Interestingly, changes in the deposition flux of O_3 are rather small, even though there is a larger amount of variability in the land surfaces and better-resolved land-sea contrast at $1^\circ \times 1^\circ$, although differences in regional deposition fluxes can be more significant. Multi-model inter-comparisons of surface deposition terms across models have shown previous versions of TM5 to be at the low end of the model spread in terms of O_3 (Hardacre et al., 2015), suggesting that the surface deposition flux to e.g. should be increased by ~10% in TM5-MP towards the multi-model mean value. This can be partly attributed to the large uncertainty which exists related to the loss of O_3 to the ocean (Hardacre et al., 2015).

Figure 3 shows comparisons of simulated and observed mass mixing ratios of surface O_3 at EMEP sites across Europe (www.emep.int; Aas et al. 2001). Previous comparisons using mCB05 have revealed high biases in surface O_3 , especially during boreal summertime (Williams et al., 2013). These high biases originate from cumulative effects associated with the accuracy of the emission inventories, the convective mixing component, the underestimation of the scattering and absorption of photolysing light due to aerosols and the chemical mechanism that is employed. For the emission component it should be noted that even at $1^\circ \times 1^\circ$ coarsening is performed, where emission inventories are typically supplied at $0.5^\circ \times 0.5^\circ$ resolution. The seasonal cycle in surface O_3 is captured to a large degree, and the high bias exhibited by the model is generally reduced by ~2-5 ppb (or ~20%) at $1^\circ \times 1^\circ$. This is associated with perturbations in the NO_x recycling terms, chemical titration by NO and convective mixing out of the boundary layer. In that the improvement in biases is largest during boreal summertime is associated with the shorter chain length of the NO_x recycling term during boreal wintertime (c.f. Fig 2). However, there is still a significant monthly-mean bias in both simulations when compared against observations throughout the year, especially for locations impacted by a large anthropogenic NO_x source. This is partly due to the low NO/ NO_2 ratio as discussed in Sect. 4 below.

Comparing vertical gradients from composites assembled from the MOZAIC measurements for DJF and JJA (Figures S7a and S7b, respectively), INTEX B (Singh et al, 2009; Figure S8) and TexAQS II (Parrish et al, 2009; Figure S9) shows that differences are small and typically mimic those which occur at the surface. There is a general positive bias of 20-40% in mixing ratios exhibited across all comparisons, although the variability in the vertical gradients across regions is captured rather well. Such positive biases have consequences for both the NO_x recycling terms and HNO_3 formation discussed in the sections below.

4 Implications for the distribution of NO and NO_2

Table 5 provides the zonally segregated annual NO_x re-cycling terms involving the main peroxy-radicals and the direct titration term involving NO for the $1^\circ \times 1^\circ$ simulation. The conversion rate of NO back into NO_2 decreases by ~2-3% across zones as a consequence of an associated increase in the titration term and re-partitioning of N



into long-lived reservoir species (see below). For the titration term involving NO, although the globally integrated flux remains relatively constant, there is contrasting behaviour for the two most important zones (TR, NH), which exhibit a lower and higher titration term, respectively. It has been shown that for regions such as Europe the increased titration results in lower surface O₃ mixing ratios (c.f. Fig. 3), improving the boreal summertime high bias at the surface.

Important model uncertainties include the quality of the MACCity NO_x emission inventory, the lifetime of NO₂ simulated in TM5 and the re-cycling term via the chemical titration of O₃. Figures 4 and 5 shows comparisons of weekly [NO] and [NO₂] surface measurements against the corresponding composites from both of the simulations, sampled at 13:00 local time close to the time of overpass for OMI and tropOMI. To supplement these comparisons we provide the seasonal mean biases for DJF and JJA from both simulations in Tables 6 and 7, respectively, calculated using weekly binned data from all EMEP sites, which measure hourly [NO] and [NO₂] levels. Here we perform an analysis across sites rather than focusing on the behaviour at selected individual locations.

For the determination of [NO₂], the reduction of NO on a Molybdenum convertor takes place with subsequent detection by chemi-luminescence, with an associated detection limit of ~0.4ppb. Previous studies have shown that some bias can result due the oxidation of nitrogen reservoirs such as PAN (Dunlea et al., 2007; Steinbacher et al., 2007). In TM5-MP all NO_x emissions are introduced as NO, although a fraction for road transport is known to be emitted directly as NO₂ (e.g. Carslaw and Beevers, 2005). Many studies have been performed comparing satellite NO₂ columns with model values, implying that inadequacies in emission inventories are somewhat region specific (e.g. Zyrichidou et al., 2015; Pope et al., 2015).

Table 6 shows a negative bias of a few $\mu\text{g m}^{-3}$ in TM5-MP in seasonal surface [NO] in Europe. This is a cumulative effect of the accuracy of the MACC NO_x emission estimates and, to a lesser extent, too high surface [O₃] (enhancing the oxidation rate of NO to NO₂). As anthropogenic emissions are the principle source of NO, no significant seasonal cycle exists in the weekly measurements, although differences in convective mixing do cause somewhat higher surface [NO] during DJF, which is often captured in TM5-MP. For ~80% of the EMEP sites we do not observe any significant change in the quality of the comparisons. For a 20% of sites, simulations of [NO] at 1° x 1° introduce significant improvements over those at 3° x 2° and seasonal variability generally improves (Fig. 4).

Table 7 shows that for [NO₂] the biases are more variable being typically in the range of $\pm 0.6 \mu\text{g m}^{-3}$, with both positive and negative biases occurring across sites. Both the conversion efficiency from NO, loss to reservoir compounds i.e. HNO₃, photo-dissociation rate and emission estimates contribute to these biases. The seasonal biases show improvements at 1° x 1° for ~35% of the EMEP sites, accompanied with degradations at ~20% of the sites. The maximal biases in [NO₂] at 1° x 1° can be approximately double those for [NO]. For the corresponding NO/NO₂ ratio, there will generally be an under-prediction in the model due to the negative biases shown for the [NO] comparisons.

Beyond Europe, we compared monthly mean TM5-MP vertical distributions of NO and NO₂ between March and May 2006 against measurements taken during the INTEx-B campaign in Figure 6. In general differences between 1° x 1° and 3° x 2° simulations are the order of a few percent, with NO₂ biased low in the lower troposphere by ~70-80%. This is partially associated with the take-off and landing of the aircraft from polluted airfields, where point sources of high anthropogenic emissions cannot be resolved at 1° x 1°. For the FT, TM5-



MP captures the observed gradient to reasonable degree. In the UT there is a consistent high bias for NO and an associated low bias for NO₂ suggesting that the conversion term is too low and the NO_x cycle is out of synch at these cold temperatures despite the addition of new reservoir species i.e. CH₃O₂NO₂.

One important gauge as to whether the chemical mechanism can capture the correct re-cycling efficiency of NO into NO₂ is to examine their ratio. These are presented in the third column of Fig. 6. In the lower troposphere (< 900 hPa) NO/NO₂ ratios of 0.1-0.2 exist which TM5-MP represents quite well, with negligible differences between 3° x 2° and 1° x 1° simulations. For the FT, TM5-MP consistently over estimates the ratio in spite of a high-bias in O₃ (c.f. Fig. 3) suggesting an exaggerated photo-dissociation rate or low bias in HO₂.

Finally in Figure 7 we show the corresponding comparisons against measurements taken during the TexasAQS-II campaign (Parrish et al, 2009) during September 2006. There is a significant underestimation in NO and NO₂, mixing ratios, with both model profiles outside the 1-σ variability of the measured mixing ratios. This is clearly related to the emission estimates for this region being underestimated in the emission inventories (e.g. Kim et al., 2011). For the resulting NO/NO₂ ratio TM5-MP captures the correct ratio in the lowest few hundred meters of the boundary layer, but overestimates the ratio at higher altitudes. In this case, the high NO and NO₂ mixing ratios at the top of the boundary layer imply that TM5-MP under-represents the NO₂ fraction, regardless of the increased recycling term related to the titration of O₃ (c.f. Table 2).

5 Changes in the NO_y budget

5.1 Long-lived reservoirs

The resolution dependent changes in the temporal distribution of [NO₂], and associated differences in VOC chemical pre-cursor emissions have the potential to alter the partitioning of reactive NO_x between the three main chemical reservoirs included in mCB05v2 (i.e. HNO₃, PAN and ORGNTR). Considering the differences in both the deposition efficiency and tropospheric lifetimes between species means the fraction of NO_x transported out of source regions could change significantly. Here we briefly examine the zonally integrated nitrogen budget terms between simulations to quantify the effect on higher spatial resolution. The seasonal distribution of these three dominant reservoir species at 1° x 1° and their individual contributions to total NO_y are shown in Figures S10 to S13 for DJF and JJA, respectively. Here we define NO_y as the cumulative total of NO, NO₂, NO₃, HNO₃, PAN, CH₃O₂NO₂, HONO, 2*N₂O₅, lumped organic nitrates and HNO₄. These are provided as reference for the reader to aid understanding of the discussion below.

Table S1 in the supplementary material provides a zonal decomposition of the tropospheric chemical budget terms for HNO₃, PAN and ORGNTR. For HNO₃, even though the recent kinetic rate parameters increase (decrease) the chemical production term at the surface (UTLS) compared to older rate data (e.g. Seltzer et al., 2015), changes in the integrated column term are small. The changes at 1° x 1° are somewhat latitude dependant (low and high NO_x regimes), with only small increases occurring in the NH and associated decreases in the tropics related to lower [OH] (i.e.) chemical production.

For PAN, both the production and destruction terms decrease marginally by ~2-3% across all zones, meaning the transport of NO_x out of the main source regions remains relatively robust. The total mass of N cycled through PAN is ~four times that of HNO₃. The changes in the production term due to temporal increases in NO₂



near high NO_x source regions (c.f. Fig. 5) are partially offset by a reduction in the mixing ratios of the acetylperoxy radical (C_2O_3 in Table 1) due to e.g. increased dry deposition of organic precursors at $1^\circ \times 1^\circ$. Although the chemical budget terms only exhibit small changes, it can be expected that the global distribution is somewhat different due the changes in the convective and advective mixing terms.

For ORGNTR, there is a 5% reduction in the production term at $1^\circ \times 1^\circ$, with an associated decrease in the loss by deposition. Both the largest production term and decrease occur in the tropics related to the strongest source being biogenic pre-cursors. Thus at $1^\circ \times 1^\circ$, this intermediate become less important as a NO_x reservoir.

Finally, the one additional intermediate not shown is $\text{CH}_3\text{O}_2\text{NO}_2$, which is primary a stable vehicle for transporting NO_x from the surface up to the UTLS, where at cold temperatures it accounts for a significant fraction of NO_2 speciation along with HNO_4 (Browne et al., 2011). At global scale three times as much nitrogen cycles through $\text{CH}_3\text{O}_2\text{NO}_2$ compared to PAN, although the thermal stability is low at temperatures $> 255^\circ\text{K}$ thus resident mixing ratios are typically small. This results in maximal mixing ratios occurring in the cold upper troposphere (up to ~ 0.2 ppb) and subsequently dissociates primarily by thermal decomposition (photolytic destruction accounting for $< 0.1\%$ of all destruction). At $1^\circ \times 1^\circ$ there is a few percent decrease in the chemical production term as a result of lower CH_3O_2 mixing ratios and more variability in the temporal temperature distribution.

Comparisons of weekly $[\text{HNO}_3]$ at the surface in Europe are shown in Figure 8 against measurements from the EMEP network. It has recently been determined that HNO_3 measurements are also sensitive to ambient nighttime N_2O_5 concentrations, which could result in a positive bias in the observations (Phillips et al., 2013). In general, the modelled seasonal cycle is not evident in the measurements, which exhibit a rather homogeneous variation in mixing ratios throughout the year typically leading to an underestimation in TM5-MP during March and an overestimation during JJA. No such seasonal pattern is observed for $[\text{NO}_2]$ (c.f. Fig. 5), thus seasonal $[\text{OH}]$ variability due to variations in photo-chemical activity and $[\text{H}_2\text{O}_{(\text{g})}]$ is a likely cause. The impact of resolution on $[\text{HNO}_3]$ is rather muted for most weeks resulting in no significant changes to the seasonal biases (not given), as constrained by the improvements in surface $[\text{NO}_2]$ (c.f. Fig. 5). The heterogeneous scavenging of HNO_3 into ammonium nitrate can act as a moderator toward gaseous HNO_3 and, although included in TM5-MP, generally produces low concentrations of e.g. ammonium nitrate (not shown). Thus, gaseous $[\text{HNO}_3]$ remains too high due to too little conversion into particles.

For other regions, we make comparisons of vertical profiles of HNO_3 and PAN between March and September 2006 against those measured during INTEX-B (Figure 9) and Texas (Figure S14). PAN is a good marker for transport in the free-troposphere due to the relatively long-lifetime at colder temperatures. For all regions the vertical gradients for both species are captured quite well, although some fine-structure is lost due to the vertical resolution of TM5-MP. This implies that the under-estimation in NO_2 (Fig. 6) is not due to lack of transport away from source regions and therefore should be more attributed to local under-estimations in emission fluxes.

Finally, we present the corresponding comparisons for September 2006 for HNO_3 and PAN measured during the TexAQS II campaign (Parrish et al., 2009) as Figure S14 in the supplementary material. For HNO_3 , although the vertical gradient is captured quite well, there is a significant low bias related to the low bias in NO_2 shown in Fig. 7, with the $1^\circ \times 1^\circ$ showing a marginal improvement in the LT for HNO_3 . For PAN the vertical profile in TM5-MP is somewhat anti-correlated around 900hPa in both simulations, with the rapid decrease at the surface not being captured by either simulation and the bias being larger for $1^\circ \times 1^\circ$.



558

559 **5.2 Short-lived reservoirs**

560

561 Here we briefly discuss the perturbations introduced for the short-lived N-reservoirs, namely HONO, HNO₄ and
 562 N₂O₅, where the chemical budget terms for all three species are provided in Table S2 in the supplementary
 563 material. For HONO it should be noted that many tropospheric CTMs have difficulty in simulating observed
 564 mixing ratios (e.g. Goncalves et al, 2012) suggesting missing (heterogeneous) source terms. The global
 565 production for HONO is an order of magnitude less than that for the other short-lived N reservoirs. At 1° x 1°
 566 there is ~10% more chemical production of HONO in high NO_x regions and no appreciable effect in the low
 567 NO_x regions. Thus the impact of increased resolution on HONO production is rather small, which is surprising
 568 considering the higher NO mixing ratios that occur in high NO_x regions (c.f. Fig 4). The muted response is due
 569 to competing oxidative processes which effectively lower the OH available for forming HONO. For HNO₄,
 570 approximately the same mass of N cycles through this species as for PAN, although the shorter lifetime means
 571 that it is more important at regional scale. Again, the impact of resolution on this species is small, where
 572 decreases in [HO₂] result in no significant net change in production for the NH. The most significant changes
 573 occur for the global production and heterogeneous conversion of N₂O₅, with enhanced chemical production of
 574 ~12% at global scale, increasing the heterogeneous sink term by ~6%, although the changes in the total mass of
 575 N converted are small. In general, this is due to an increase in the production of the NO₃ radical by ~10% at 1° x
 576 1° (not shown) resulting in enhanced N₂O₅ mixing ratios.

577

578 **6 Implications for tropospheric CH₂O retrieval**

579

580 The implications of higher resolution for the global distribution of CH₂O are rather modest. In Table 8, we show
 581 zonally integrated chemical production and destruction terms for CH₂O, which suggests changes of the order of
 582 a few percent at global scale. The most notable difference is the increase in the cumulative deposition term of
 583 ~4% at 1° x 1°, thus reducing the atmospheric lifetime of CH₂O in TM5-MP. Again this low impact shows that
 584 the increase in the temporal variability of the meteorological data at 1° x 1°, and thus the local variability of
 585 cloud Surface Area Data, only changes the net deposition term by a few percent. Even though the temporal
 586 distribution of the surface mixing ratios shows more variability at 1° x 1° due to the better representation of
 587 regional pre-cursor sources terms (e.g.) isoprene and terpene, only moderate improvements occur to the
 588 simulated profiles and total columns due to changes in transport. For instance, when analysing individual
 589 production terms (not given) for the tropics, decreases are related to small changes in the dominating chemical
 590 source terms (e.g. oxidation of CH₃OOH; ~3-5 Tg less CH₂O yr⁻¹). For the chemical destruction term, the
 591 relative insensitivity of the photolysis of CH₂O towards resolution (similar to J_{O3}; c.f. Fig S4) results in small net
 592 decreases in line with changes in the chemical production term.

593 Figure 10 compares monthly mean tropospheric profiles of CH₂O measured during INTEX-B (Singh et al.,
 594 2009) with those from both TM5-MP simulations for March to May 2006. In general, there is a fair
 595 representation of the vertical gradient of CH₂O by TM5-MP for all months shown, although surface mixing
 596 ratios are typically too high suggesting loss by deposition is under-estimated or that the chemical production
 597 term is too. Moreover, there appears to be a missing (chemical) source term in the UTLS in TM5-MP leading to



a ~ 30-50% (~0.05 ppb) low bias above 600hPa, therefore no significant improvement to the under-estimation in the SH CH₂O column in TM5-MP occurs compared to previous versions (Zeng et al, 2015). Comparing profiles shows that the changes in the vertical distribution of CH₂O at 1° x 1° are minimal in the chemical background compared to 3° x 2°, with the main differences originating from more efficient transport out of source regions (c.f. March). These findings are further confirmed by the comparisons of TM5-MP against TexAQS II measurements for September 2006 (Figure S13).

7 Implications for tropospheric SO₂ retrieval

In Figure 11, we compare weekly [SO₂] for 2006 at number of EMEP sites in Austria (AT02, Forest), the Netherlands (NL09, Rural), Great Britain (GB43, Rural) and Spain (ES10, Rural), with most being positioned away from strong point sources. For SO₂ in Europe, the main source is primarily anthropogenic (e.g. Energy Sector) followed by oxidation to sulphate, with the tropospheric lifetime varying from ~2 days during winter and ~19 hours during summer (Lee et al, 2011). High [SO₂] has been observed throughout the EMEP network in e.g. The Netherlands and Spain, which is significantly higher than that measured in Central Europe (Tørseth et al., 2012). Although the measurement uncertainty is somewhat site specific due to the different methodology employed, it is typically around ~1.3 ug/m³ (e.g. Hamad et al., 2010). Comparing weekly averages shows that for most sites shown there is a significant low bias at 3° x 2°, indicating inaccuracies in the MACC emission inventory and the effect of coarsening to the model resolution. At 1° x 1° significant improvements occur as a result of the better temporal resolution of the emission sources.

Table 9 provides an overview of the changes in the seasonal biases for all of the EMEP sites that measure hourly [SO₂], with the biases calculated for the overpass time of tropOMI aggregated on a weekly basis. Improvements occur at 1° x 1° for ~20% of the sites during both seasons, with the majority (~50%) of sites showing no significant improvement (< 5%). In such instances the local [SO₂] is determined more by long-range transport (thus sensitive to wash-out) rather than a local emission source, where strong mitigation practises have been implemented in Europe over the last few decades reducing resident [SO₂] significantly (Tørseth et al., 2012). For some sites there is a notable increase in biases at 1° x 1° (20% DJF, 25% JJA) indicating that too strong local emission sources occur in the MACC inventories (e.g. ES13 and GR01). For others (e.g. ES08 and NL07) significantly low biases occur suggesting the opposite problem.

Finally, for the vertical profiles we make comparisons against monthly mean composites assembled from measurements taken during INTEX-B (Figure S14) and TexAQS II (Figure 12) as for the other trace species. For the more pristine locations there are typically low biases at 3° x 2° for all months, especially at the surface during March indicating a significant under-estimation in the emission fluxes of SO₂. Increasing to 1° x 1° only provides an improved correlation for March, due to the transport in the FT being described better as for that shown for NO₂ in Fig. 6. For April, the comparison shows a significant underestimation in the column for both simulations, where corresponding comparisons of the vertical profiles of Di-Methyl Sulphide, which acts as a key source of SO₂ in the Equatorial Pacific (Alonza Gray et al., 2011), also show significant low biases (not shown). For May again no significant improvement occurs, although both simulations capture the peak in SO₂ mixing ratios at the top of the boundary layer. More relevant for satellite based retrievals is the observed column near strong anthropogenic source regions as shown in Figure 13 over Texas during September 2006. Here a clear



improvement occurs at $1^\circ \times 1^\circ$, with the low bias in the boundary layer being reduced significantly although the integrated column is still too low. Again this is due to the under-estimation in the source emission fluxes in the anthropogenic emission inventory employed.

8 Conclusions

In this paper we have provided a comprehensive description of the high-resolution $1^\circ \times 1^\circ$ version of TM5, which is to be used for the purpose of providing *a-priori* columns for the satellite retrieval of trace gas columns of NO_2 , CH_2O and SO_2 . By performing identical simulations at both $3^\circ \times 2^\circ$ and $1^\circ \times 1^\circ$ horizontal resolution and comparing the resulting global distributions of trace gas species, photolysis frequencies and chemical budget terms, we quantify and validate both the near-surface and vertical distributions for the evaluation year of 2006.

Comparing the seasonal distribution in ^{222}Rn shows that differences of $\pm 20\%$ occur at global scale, with significantly larger differences for specific coastal regions and tropical oceans. In order to assess the changes in convective activity above strong NO_x sources, we show that differences of between $\sim 2\text{--}10\%$ ($\sim 10\text{--}20\%$) exist for the Northern mid-latitudes (tropics) at higher resolution, with both weaker and stronger upwelling occurring depending on the region and the season. The differences are site specific being affected by location orography.

The impact on global monthly mean J_{O_3} and J_{NO_2} surface values over a range of conditions is limited to $\sim 2\%$ and $\sim 5\text{--}10\%$, respectively. This is surprising considering the larger variability in cloud cover and surface albedo at $1^\circ \times 1^\circ$. Examining changes in J_{O_3} and J_{NO_2} which occur throughout the tropospheric column reveals that significant differences of $>10\%$ can occur at the top of the boundary layer at tropical locations. Such modest changes associated with this dominant loss term result in the change in the integrated chemical budget terms to be rather low.

Analysing the chemical budget terms for tropospheric O_3 shows (i) a reduction in the Stratosphere-Troposphere exchange flux of $\sim 7\%$ to $597 \text{ Tg O}_3 \text{ yr}^{-1}$, (ii) a repartitioning of the contribution from Stratospheric down welling in both the Northern and Southern hemispheres, (iii) no significant change in the tropospheric burden of O_3 and (iv) modest changes in the integrated chemical production and destruction terms. Comparing simulated mixing ratios against surface measurements in Europe shows that the positive bias present in TM5 decreases by $\sim 20\%$ at $1^\circ \times 1^\circ$ between $2\text{--}5 \text{ ppb month}^{-1}$. This bias persists throughout the vertical column across diverse global regions, although the vertical gradient in tropospheric O_3 is captured quite well.

For NO and NO_2 increasing horizontal resolution results in only modest differences in the zonal mean recycling terms and the loss of O_3 by chemical titration. Comparisons against surface measurements in Europe shows that there is a consistent negative bias in NO weekly concentrations of a few $\mu\text{g m}^{-3}$ associated with both too high surface O_3 (enhanced NO titration) and the accuracy of the emission inventories. For NO_2 , the biases in the weekly concentrations are larger and can be both positive and negative. Increasing horizontal resolution has little effect on improving the NO biases, but results in improvements for NO_2 at $\sim 35\%$ of the available sites, with $\sim 45\%$ of sites showing limited changes. For the tropospheric column the improvement in the comparisons in only a of the order of few percent, with a significant under-estimation in both NO and NO_2 throughout the tropospheric column. Analysing the NO/NO_2 ratio and comparing against observations shows that although partitioning is captured in the boundary layer there is a significant overestimation in the upper troposphere.



Finally for CH_2O and SO_2 , which can also be retrieved from satellite measurements, the effect of increased resolution is rather modest due to compensating changes towards the chemical budget terms. When compared against observations there is a persistent low bias for tropospheric CH_2O due to missing production terms especially on the Free Troposphere. For SO_2 comparison with surface observations in Europe show lower biases at ~20% of sites due to more accurate local emission fluxes, whereas for the majority of cases (~50%) there is no significant change. Comparing vertical profiles shows a significant under-estimation in the tropospheric column likely associated with either precursors or direct emission terms.

Code Availability

The TM5-MP code can be downloaded from the SVN server hosted at KNMI, The Netherlands. A request to generate a new user account for access can be made by e-mailing sager@knmi.nl. Any new user groups need to agree to the protocol set out for use, where it is expected that any developments are accessible to all users after publication of results. Attendance at 9-monthly TM5 international meetings is encouraged to avoid duplicity and conflict of interests.

Acknowledgements

We thank M. van Weele for processing the MSR2 stratospheric ozone data record used for constraining the overhead O_3 field and T. P. C. van Noije for updating the SO_x emission estimates. We thank V. Huijnen for providing estimates on the heterogeneous uptake co-efficients.



Table 1: Details of the reaction rate data applied for NO_x radical-radical reactions and nitrogen reservoirs. The k₀ terms are multiplied by the relevant air density to calculate the correct forward and backward rate constants. The reaction data and stoichiometry is taken from Atkinson et al. (2004) accommodating the latest evaluation at <http://iupac.pole-ether.fr>.

Reactants	Products	Rate parameters
NO + O ₃	NO ₂	$3.0 \times 10^{-12} \cdot \exp(-1500/T)$
NO ₂ + O ₃	NO ₃	$1.4 \times 10^{-13} \cdot \exp(-2470/T)$
NO + HO ₂	NO ₂ + OH	$3.3 \times 10^{-12} \cdot \exp(270/T)$
NO + CH ₃ O ₂	CH ₂ O + HO ₂ + NO ₂	$2.8 \times 10^{-12} \cdot \exp(300/T)$
OH + NO ₂	HNO ₃	$k_0 = 3.2 \times 10^{-30} \cdot (300/T)^{4.5}$ $k_\infty = 3.0 \times 10^{-11}$
NO + NO ₃	NO ₂ + NO ₂	$1.8 \times 10^{-11} \cdot \exp(110/T)$
NO ₂ + NO ₃	N ₂ O ₅	$k_0 = 8.0 \times 10^{-27} \cdot (300/T)^{3.5}$ $k_\infty = 3.0 \times 10^{-11} \cdot (300/T)^{1.0}$
N ₂ O ₅ + M	NO ₂ + NO ₃	$k_0 = 1.3 \times 10^{-3} \cdot (300/T)^{3.5} \cdot \exp(-11000/T)$ $k_\infty = 9.7 \times 10^{-14} \cdot (300/T)^{-0.1} \cdot \exp(-11080/T)$
HO ₂ + NO ₂	HNO ₄	$k_0 = 1.4 \times 10^{-31} \cdot (300/T)^{3.1}$ $k_\infty = 4.0 \times 10^{-12}$
HNO ₄ + M	HO ₂ + NO ₂	$k_0 = 4.1 \times 10^{-5} \cdot \exp(-10650/T)$ $k_\infty = 6.0 \times 10^{15} \cdot \exp(-11170/T)$
OH + HNO ₄	NO ₂	$1.3 \times 10^{-12} \cdot \exp(380/T)$
OH + NO + M	HONO	$k_0 = 7.0 \times 10^{-31} \cdot (300/T)^{4.4}$ $k_\infty = 3.6 \times 10^{-11} \cdot (300/T)^{0.1}$
HONO + hν	OH + NO	
OH + HONO	NO ₂	$2.5 \times 10^{-12} \cdot \exp(260/T)$
NO ₂ + CH ₃ C(O)O ₂	PAN	$k_0 = 3.28 \times 10^{-28} \cdot (300/T)^{6.87}$ $k_\infty = 1.125 \times 10^{-11} \cdot (300/T)^{1.105}$
PAN	NO ₂ + CH ₃ C(O)O ₂	$k_0 = 1.1 \times 10^{-5} \cdot \exp(-10100/T)$ $k_\infty = 1.9 \times 10^{17} \cdot \exp(-14100/T)$



20

PAN + hν	CH ₃ C(O)O ₂ + NO ₂	
	CH ₃ O ₂ + NO ₃	
CH ₃ O ₂ + NO ₂	CH ₃ O ₂ NO ₂	k ₀ = 2.5 × 10 ⁻³⁰ × (300/T)
		k _∞ = 1.8 × 10 ⁻¹¹
CH ₃ O ₂ NO ₂	CH ₃ O ₂ + NO ₂	k ₀ = 9.0 × 10 ⁻⁵ × exp(-9690/T)
		k _∞ = 1.1 × 10 ¹⁶ × exp(-10560/T)
NO ₃ + HO ₂	HNO ₃	4.0 × 10 ⁻¹²

701
 702



Table 2: Details of updates made to the reaction data and stoichiometry of the modified CB05 chemical mechanism for other reactions. Data is taken from the following: [1] Atkinson et al. (2004) accommodating the latest evaluation at <http://iupac.pole-ether.fr>, [2] Branching ratio (R) equal to $1/(1+498 \cdot \exp(-1160/T))$, [3] Yarwood et al. (2005), [4] Sander et al. (2011), [5], Atkinson et al. (2006), [6] Emmons et al. (2010), [7] Hauglustaine et al. (2014), [8] Rate assumed equal to NH_2 analogue, [9] assumed to be equal to HNO_4 after Browne et al. (2011).

Reactants	Products	Rate expression	Ref.
$\text{CH}_3\text{O}_2 + \text{HO}_2$	CH_3OOH	$3.8 \times 10^{-13} \cdot \exp(750/T) \cdot R$	[1],[2]
$\text{CH}_3\text{O}_2 + \text{HO}_2$	CH_2O	$3.8 \times 10^{-13} \cdot \exp(750/T) \cdot (1-R)$	[1],[2]
$\text{CH}_3\text{O}_2 + \text{CH}_3\text{O}_2$	$1.37\text{CH}_2\text{O} + 0.74\text{HO}_2 + 0.63\text{CH}_3\text{OH}$	$9.5 \times 10^{-14} \cdot \exp(390/T)$	[3],[4]
$\text{OH} + \text{C}_3\text{H}_8$	$\text{IC}_3\text{H}_7\text{O}_2$	$7.6 \times 10^{-12} \cdot \exp(-585/T)$	[5],[6]
$\text{NO} + \text{IC}_3\text{H}_7\text{O}_2$	$0.82\text{CH}_3\text{COCH}_3 + \text{HO}_2 + 0.27\text{ALD2} + \text{NO}_2$	$4.2 \times 10^{-12} \cdot \exp(180/T)$	[6]
$\text{HO}_2 + \text{IC}_3\text{H}_7\text{O}_2$	ROOH	$7.5 \times 10^{-13} \cdot \exp(700/T)$	[6]
$\text{OH} + \text{C}_3\text{H}_6$	$\text{C}_3\text{H}_6\text{O}_2$	$k_0 = 8.0 \times 10^{-27} \cdot (-300/T)^{3.5}$ $k_\infty = 3.0 \times 10^{-11} \cdot (-300/T)^{1.0}$	[5],[6]
$\text{NO}_3 + \text{C}_5\text{H}_8$	$0.2\text{ISPD} + \text{XO}_2 + 0.8\text{HO}_2 + 0.8\text{ORGNTNTR} + 0.8\text{ALD2} + 2.4\text{PAR} + 0.2\text{NO}_2$	$2.95 \times 10^{-12} \cdot \exp(465/T)$	[5]
$\text{NO} + \text{C}_3\text{H}_6\text{O}_2$	$\text{ALD2} + \text{CH}_2\text{O} + \text{HO}_2 + \text{NO}_2$	$4.2 \times 10^{-12} \cdot \exp(180/T)$	[6]
$\text{HO}_2 + \text{C}_3\text{H}_6\text{O}_2$	ROOH	$7.5 \times 10^{-13} \cdot \exp(700/T)$	[6]
$\text{NO}_3 + \text{DMS}$	$\text{SO}_2 + \text{HNO}_3$	$1.9 \times 10^{-13} \cdot \exp(520/T)$	[1]
$\text{NH}_2 + \text{OH}$		3.4×10^{-11}	[E]
$\text{NH}_2 + \text{HO}_2$	NH_3	3.4×10^{-11}	[4],[7]
$\text{NH}_2 + \text{O}_3$	NH_2O_2	$4.3 \times 10^{-12} \cdot \exp(-930/T)$	[4],[7]
$\text{NH}_2 + \text{O}_2$	NO	6.0×10^{-21}	[1],[7]
$\text{NH}_2\text{O}_2 + \text{NO}$	$\text{NH}_2 + \text{NO}_2$	$4.0 \times 10^{-12} \cdot \exp(450/T)$	[7],[8]
$\text{NH}_2\text{O}_2 + \text{O}_3$	NH_2	$4.3 \times 10^{-12} \cdot \exp(-930/T)$	[7],[8]
$\text{NH}_2\text{O}_2 + \text{HO}_2$	NH_2	3.4×10^{-11}	[8]
$\text{CH}_3\text{O}_2\text{NO}_2 + h\nu$	$\text{CH}_3\text{O}_2 + \text{NO}_2$		[9]



	$\text{CH}_3\text{O}_2\text{NO}_2 + h\nu$	$\text{CH}_2\text{O} + \text{HO}_2 + \text{NO}_3$	[9]
	$\text{HO}_2 + \text{aero}$	$0.5\text{H}_2\text{O}_2$	
	$\text{NO}_3 + \text{aero}$	HNO_3	[6]
710	<hr/>		
711			



Table 3: The zonally segregated emission totals introduced into TM5-MP for the year 2006. All organic hydrocarbons are given in Tg C yr⁻¹, except for CO, CH₂O and CH₃OH and all NO_x emissions are introduced as NO. No direct emissions occur for HNO₃, PAN, ORGNTR, HONO, N₂O₅, NO₂, CH₃O₂NO₂ or O₃.

Species (Tg/Year)	Global	30-90°S	30S-30°N	30-90°N
CO	1081.0	24.4	755.1	301.27
NO _x (as N)	49.0	1.5	24.0	23.6
SO ₂	117.0	3.0	49.2	64.3
DMS (as S)	19.2	6.7	9.3	3.2
NH ₃	56.6	3.1	27.9	25.6
CH ₂ O	13.5	0.3	10.5	2.7
PAR	34.1	0.7	18.5	14.9
OLE	22.4	0.9	16.6	4.9
ALD2	13.4	0.4	11.2	1.8
CH ₃ CHCHO	2.2	0.0	1.2	1.0
CH ₃ OH	100.7	3.3	82.5	14.9
CH ₃ CH ₂ OH	70.4	2.8	52.6	15.1
C ₂ H ₄	25.9	1.0	19.0	5.9
C ₂ H ₆	6.1	0.3	5.3	1.5
C ₃ H ₈	5.6	0.4	3.6	1.6
C ₃ H ₆	19.6	0.9	14.8	3.9
CH ₃ COCH ₃	27.4	0.8	22.0	4.6
HCOOH	1.8	0.0	1.5	0.3
CH ₃ COOH	7.1	0.1	6.0	1.0
C ₅ H ₈	510.0	23.2	441.9	45.0
C ₁₀ H ₁₆	85.4	2.3	70.2	12.9



719

720 Table 4: The tropospheric chemical budget terms for O_3 during 2006 for the $1^\circ \times 1^\circ$ simulation given in
 721 $Tg\ O_3\ yr^{-1}$. The associated percentage changes are given when comparing against the $3^\circ \times 2^\circ$ simulation
 722 ($1^\circ \times 1^\circ/3^\circ \times 2^\circ$). The definition of the chemical tropopause and the calculation of the STE are defined
 723 using the methodology outlined in Stevenson et al. (2006). The stratospheric nudging term refers to
 724 total change in the mass of O_3 in the stratospheric column when nudging towards observational
 725 constraints from the MSR (Huijnen et al., 2010). The contribution to each term from the SH extra-
 726 tropics/tropics/NH extra-tropics (defined as $90-30^\circ S/30^\circ S-30^\circ N/30-90^\circ N$) are provided. The fraction of
 727 the tropospheric burden originating from the stratosphere is also given.

728

Term	Global	%	SH	%	Tropics	%	NH	%
Net STE	579	-6.7	166		396		16	
Strat. Nudging	1440	-0.7	-224	2.8	1615	-	49	5.8
Trop.Chem.Prod	5532	-1.9	389	-2.2	3938	-3.5	1206	-2.2
Trop.Chem.Loss	5162	-2.4	440	-1.0	3869	-2.5	853	-2.8
BO_3	378	-2.0	72	1.7	203	-2.3	104	-3.4
Strat BO_3	80	-2.0	23	9.1	38	-6.5	24	-2.0
Deposition	949	0.8	115	0.6	465	-	369	1.9
O_3S Deposition	97	5.0	19	7.5	37	-1.2	42	10.0

729

730

731 Table 5: The annual NO to NO_2 re-cycling terms involving peroxy-radicals given in $Tg\ N\ yr^{-1}$ for 2006
 732 at $1^\circ \times 1^\circ$ resolution. In mCB05v2 XO_2 represents lumped alkyl-peroxy radicals (Yarwood et al, 2005).
 733 The RO_2 term is an aggregate of numerous specific peroxy-radical conversion terms in the modified
 734 CB05 mechanism (Williams et al., 2013; Tables 1 and 2). Also provided are the approximate
 735 percentage differences when comparing with $3^\circ \times 2^\circ$ ($1^\circ \times 1^\circ/3^\circ \times 2^\circ$). The chemical tropopause is
 736 defined using the methodology outline in Stevenson et al. (2006).

737

Reaction	Global	%	SH	%	Tropics	%	NH	%
$NO + HO_2$	1058	-1.2	79	-1.2	740	-1.9	239	0.8
$NO + CH_3O_2$	407	-2.2	31	-2.6	294	-2.8	82	-2.0
$NO + XO_2$	147	-2.1	7	-3.6	111	-2.6	29	-
$NO + RO_2$	9.4	-4.4	0.4	-2.6	6.3	-4.4	2.7	-4.2
$NO + O_3$	5403	0.1	518	7.5	2933	-3.9	1953	4.9

738

739



Table 6: The seasonal mean absolute biases of weekly [NO] ($\mu\text{g m}^{-3}$) composed from daily measurements at 13:00 for DJF and JJA (measurements-model). Values are shown for both the $3^\circ \times 2^\circ$ and $1^\circ \times 1^\circ$ simulations. Those with differences $< 5\%$ are considered to exhibit no discernible change in the bias.

EMEP Station	Lat	Lon	DJF $3^\circ \times 2^\circ$	DJF $1^\circ \times 1^\circ$	JJA $3^\circ \times 2^\circ$	JJA $1^\circ \times 1^\circ$
CH01	46.32	7.59	-0.01	-0.01	0.00	-0.01
CZ03	49.35	15.50	-4.05	-3.30	-1.61	-1.35
DE43	47.48	11.10	-2.37	-2.36	-0.47	-0.48
DK05	54.44	10.44	-2.51	-2.61	-1.29	-1.51
ES07	58.23	21.49	-3.80	-3.84	-1.45	-1.48
ES08	43.26	-4.51	-2.08	-2.09	-1.00	-1.01
ES09	41.16	-3.80	-0.93	-0.93	-1.07	-1.07
ES10	38.28	3.19	-1.14	-1.24	-0.75	-0.88
ES11	39.50	-6.55	-1.07	-1.07	-0.44	-0.45
ES12	41.17	-1.60	-1.34	-1.34	-0.95	-0.95
ES13	41.24	-5.52	-2.50	-1.90	-0.74	-0.62
ES14	39.31	0.43	-2.21	-2.20	-1.27	-1.27
ES15	43.13	-4.21	-1.62	-1.61	-0.99	-1.00
ES16	43.37	-7.41	-2.39	-2.39	-1.11	-1.11
FR13	46.39	0.11	-1.90	-1.94	-0.52	-0.52
FR15	55.18	0.45	-3.09	-3.04	-1.51	-1.58
GB02	50.35	-3.12	-1.23	-1.23	-0.93	-0.92
GB13	54.20	-3.42	-1.28	-1.32	-0.58	-0.55
GB14	52.30	-0.48	-3.03	-3.04	-0.98	-0.98
GB31	53.23	-3.11	-1.74	-1.74	-0.90	-0.91
GB37	50.47	-1.45	-3.09	-3.08	-1.22	-1.21
GB38	51.13	0.10	-2.87	-2.78	-1.92	-1.72
GB44	51.17	-3.20	-1.65	-1.45	-0.27	-0.67
GB45	52.17	0.17	-1.80	0.11	0.20	0.19
GB51	52.33	0.46	-3.68	-3.42	-1.29	-1.17
NL91	52.18	4.30	-4.47	-3.51	-1.98	-1.86



750 Table 7: As for Table 5 except for NO₂.
 751

EMEP Station	Lat	Lon	DJF 3° x 2°	DJF 1° x 1°	JJA 3° x 2°	JJA 1° x 1°
BE32	50.30	4.59	10.56	1.27	1.69	-2.13
CH01	46.32	7.59	-0.04	-0.03	-0.02	-0.01
CZ03	49.35	15.50	-4.04	0.03	-1.62	0.34
DE43	47.48	11.10	-2.37	-2.36	-0.49	-0.48
DK05	54.44	10.44	6.07	5.56	1.04	-0.02
ES07	58.23	21.49	-1.13	-1.79	-0.96	-1.15
ES08	43.26	-4.51	-2.01	-2.10	-0.93	-1.01
ES09	41.16	-3.80	-0.95	-0.94	-1.07	-1.07
ES10	42.19	3.19	2.18	1.46	0.92	-0.01
ES11	38.28	-6.55	-1.08	-1.08	-0.44	-0.44
ES12	39.50	-1.60	-1.36	-1.35	-0.95	-0.95
ES13	41.17	-5.52	-2.51	-0.29	-0.74	0.19
ES14	41.24	0.43	-2.22	-2.21	-1.27	-1.26
ES15	39.31	-4.21	-1.64	-1.63	-0.99	-0.99
ES16	43.13	-7.41	-2.40	-2.39	-1.11	-1.11
FI09	59.46	21.22	0.79	-0.91	-0.10	-0.53
FI37	60.31	27.41	10.04	9.60	1.70	0.92
FI96	62.35	24.11	0.40	0.34	0.31	0.17
FR13	68.00	24.09	-1.96	-1.95	-0.54	-0.54
FR15	43.37	0.11	-3.84	-3.91	-1.78	-1.81
GB02	46.39	0.45	3.12	3.42	0.82	0.54
GB13	55.18	-3.12	-2.17	-2.13	-1.00	-0.98
GB14	50.35	-3.42	5.02	3.93	1.17	1.50
GB31	54.20	-0.48	-1.71	-1.71	-0.90	-0.90
GB37	52.30	-3.11	-3.10	-3.08	-1.25	-1.25
GB38	53.23	-1.45	-4.05	-4.03	-2.20	-2.19
GB44	50.47	0.10	6.21	6.69	0.61	1.42
GB45	51.13	-3.20	6.28	6.00	3.48	1.94
GB51	52.17	-0.17	12.56	16.60	4.11	4.50
GR01	41.45	42.49	0.50	2.07	0.40	1.05
NL09	53.2	6.16	-3.21	-1.63	-1.18	-0.19
NL10	51.32	5.51	3.48	3.52	0.92	-0.29
NL91	52.18	4.30	11.81	6.42	1.48	-0.81

752
 753



754

755 Table 8: The tropospheric chemical budget for the CH₂O given in Tg CH₂O yr⁻¹ during 2006 for the 1° x
 756 1° simulation. Percentage differences are shown against the corresponding 3° x 2° simulation.
 757

Budget Term	Global	%	SH	%	Tropics	%	NH	%
CH ₂ O CP	1919	-1.1	147	-0.3	1491	-1.0	281	-2.0
CH ₂ O CD	1739	-1.6	134	-0.5	1349	-1.1	256	-2.3
CH ₂ O Dep.	193	3.1	15	2.0	149	3.9	29	-

758

759 Table 9: The seasonal mean biases of daily [SO₂] (µg m⁻³) at 13:00 for DJF and JJA, when taking the
 760 difference between measurements-model values. Values are shown for both the 3° x 2° and 1° x 1°
 761 simulations. Those with differences < 5% are considered to exhibit no discernible change in the bias.
 762

EMEP Station	Lat	Lon	DJF 3° x 2°	DJF 1° x 1°	JJA 3° x 2°	JJA 1° x 1°
AT02	47.46	16.46	-3.34	-3.15	-0.89	-0.53
AT05	46.40	12.58	-0.42	-0.41	-0.14	-0.14
AT48	47.50	14.26	-0.64	-0.63	-0.14	-0.15
CZ03	49.35	15.50	-3.52	3.65	-0.69	0.64
ES07	58.23	21.49	1.22	0.73	0.38	0.31
ES08	43.26	-4.51	-2.98	-3.21	-1.19	-1.58
ES09	41.16	-3.80	-0.62	-0.61	-0.42	-0.42
ES10	42.19	3.19	2.37	2.45	1.93	1.53
ES11	38.28	-6.55	-0.63	-0.61	-0.70	-0.70
ES12	39.50	-1.60	-0.47	-0.45	-0.32	-0.32
ES13	41.17	-5.52	-0.81	2.71	-0.78	0.55
ES14	41.24	0.43	-0.70	-0.67	-0.47	-0.47
ES15	39.31	-4.21	-0.40	-0.37	-0.45	-0.46
ES16	43.13	-7.41	-3.84	-3.82	-1.66	-1.66
GB37	52.30	-3.11	-2.92	-2.91	-1.72	-1.72
GB38	53.23	-1.45	2.93	2.75	0.39	1.33
GB43	51.14	-4.42	-1.49	4.77	-2.03	-0.63
GB45	52.17	-0.17	3.87	7.20	1.01	1.77
GR01	38.22	23.50	1.70	2.77	0.74	1.50
NL07	52.50	6.34	2.58	-1.67	0.46	-1.03
NL08	52.70	5.12	1.77	1.56	-0.14	-0.30
NL09	53.2	6.16	2.53	2.16	0.47	0.27

763



28

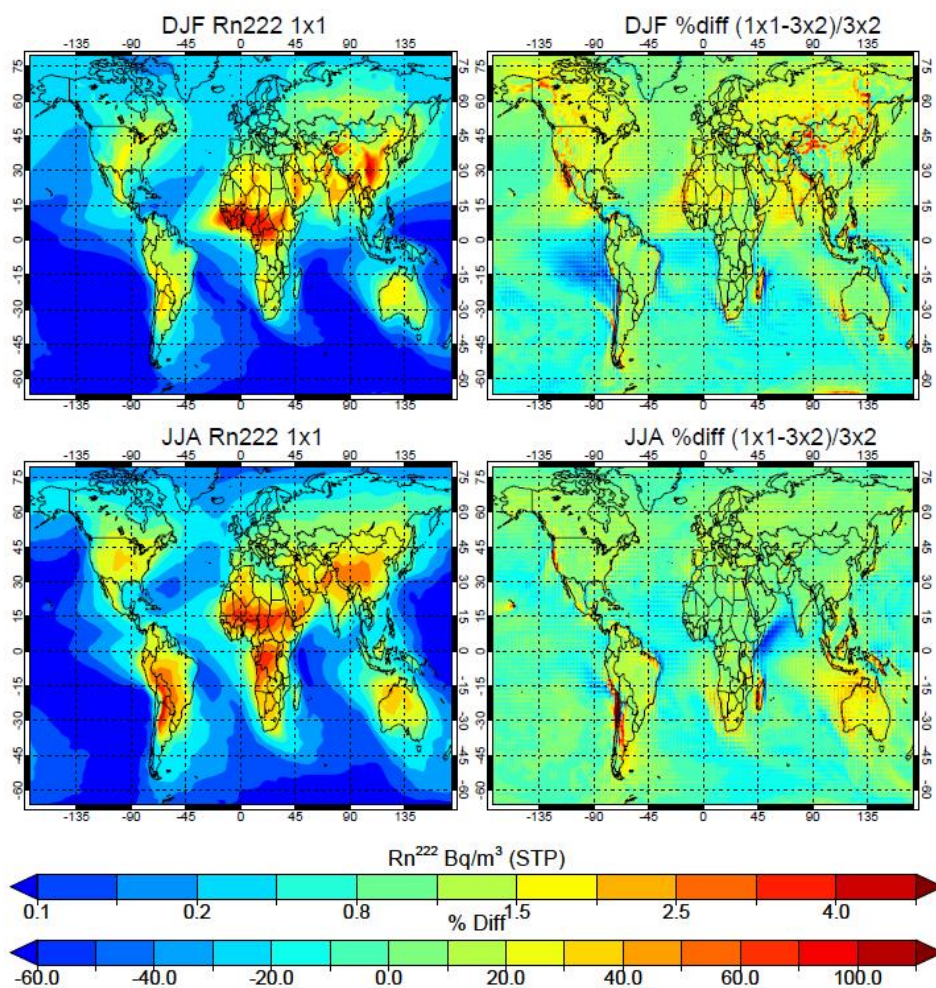


Figure 1: The seasonal distributions of Rn^{222} between 800-900hPa for DJF (top) and JJA (bottom) for the $1^\circ \times 1^\circ$ (right) simulation, with the associated percentage differences when compared against the $3^\circ \times 2^\circ$ simulation.

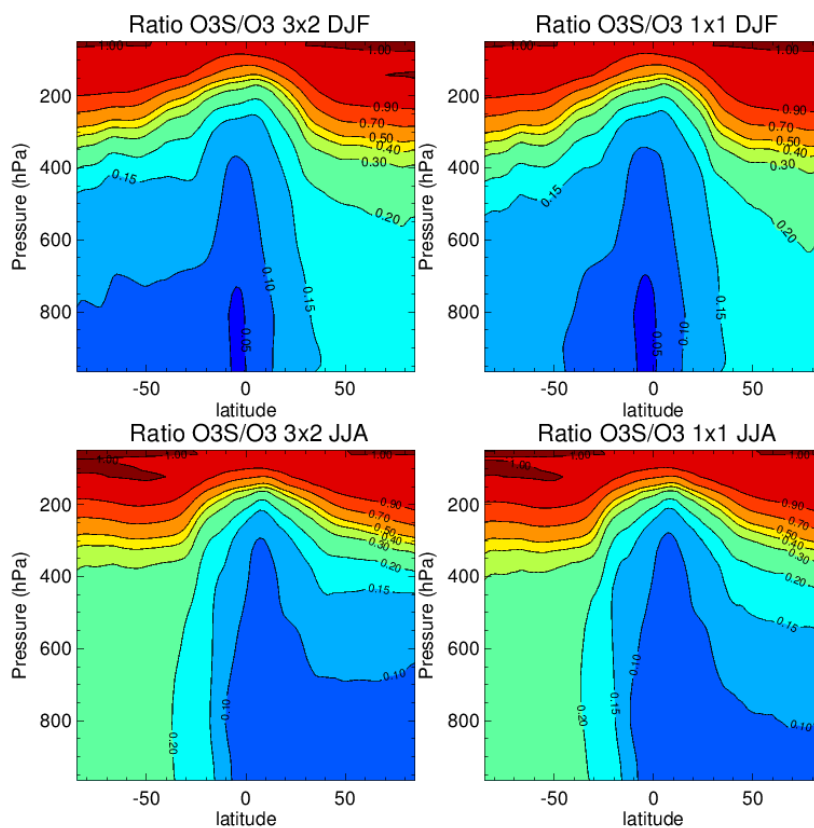
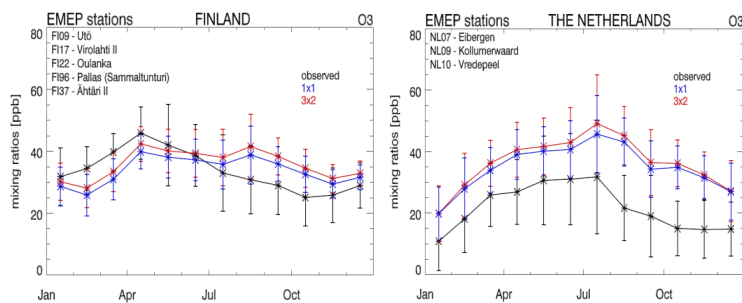


Figure 2: Zonal mean seasonal distribution of the TM5-MP O_3S/O_3 ratio for the $3^\circ \times 2^\circ$ (left) and $1^\circ \times 1^\circ$ (right) simulations.

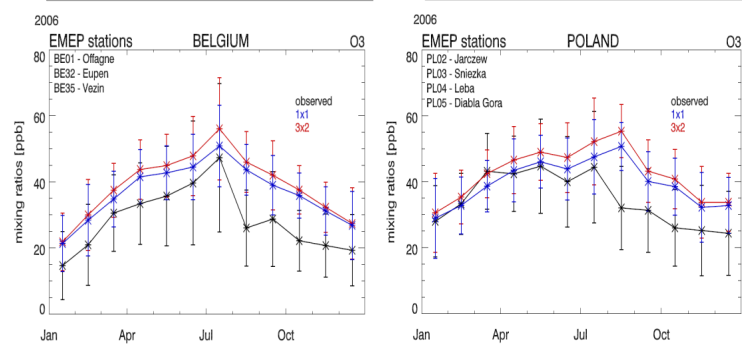


30

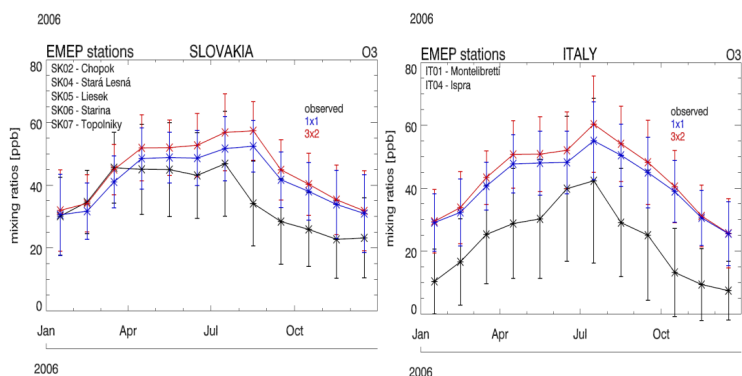
776



777



778



779

780

781

782

783

784

785

786

787

Figure 3: Comparisons of the seasonal variability in TM5-MP mass mixing ratios for surface O_3 against composites of measurements taken across the EMEP monitoring network for 2006. Both the co-located TM5-MP $3^\circ \times 2^\circ$ and $1^\circ \times 1^\circ$ monthly mean values are shown, along with the $1-\sigma$ variability for Finland, The Netherlands, Belgium, Poland, Slovakia and Italy. Individual stations that are aggregated are given in the panels.

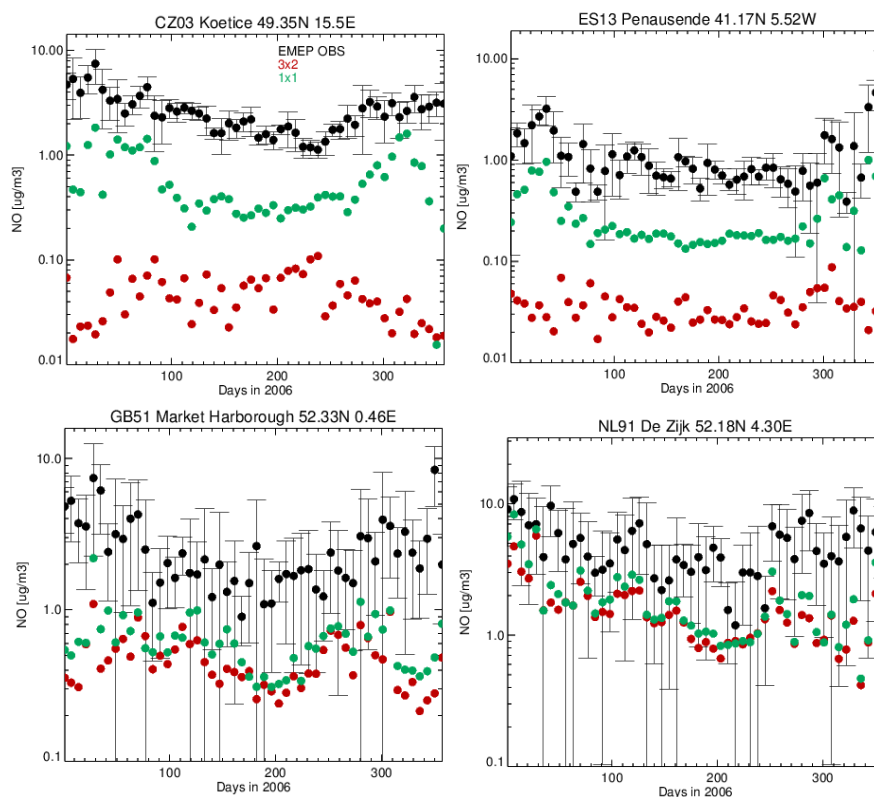


Figure 4: Comparison of TM5-MP weekly NO surface concentrations sampled at 13:00 UT each day during 2006 with observed NO surface concentrations ($\mu\text{g m}^{-3}$). The selected sites shown are in the Czech Republic (top left), Spain (top right), Great Britain (bottom left) and The Netherlands (bottom right).



32

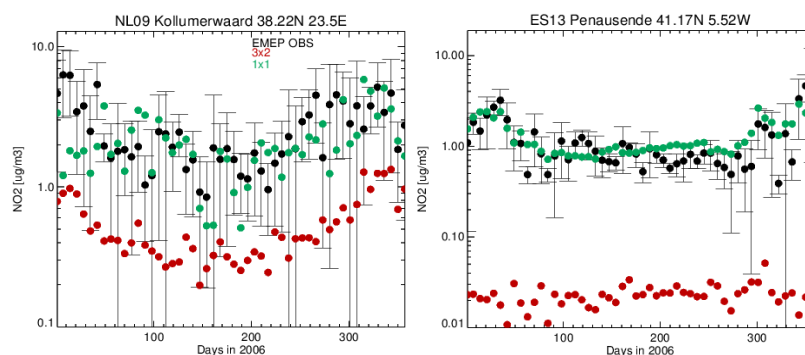


Figure 5: Comparison of weekly TM5-MP NO₂ surface concentrations sampled at 13:00 UT each day during 2006 with observed NO₂ surface concentrations ($\mu\text{g m}^{-3}$). The selected sites shown are in The Netherlands (left) and Spain (right).

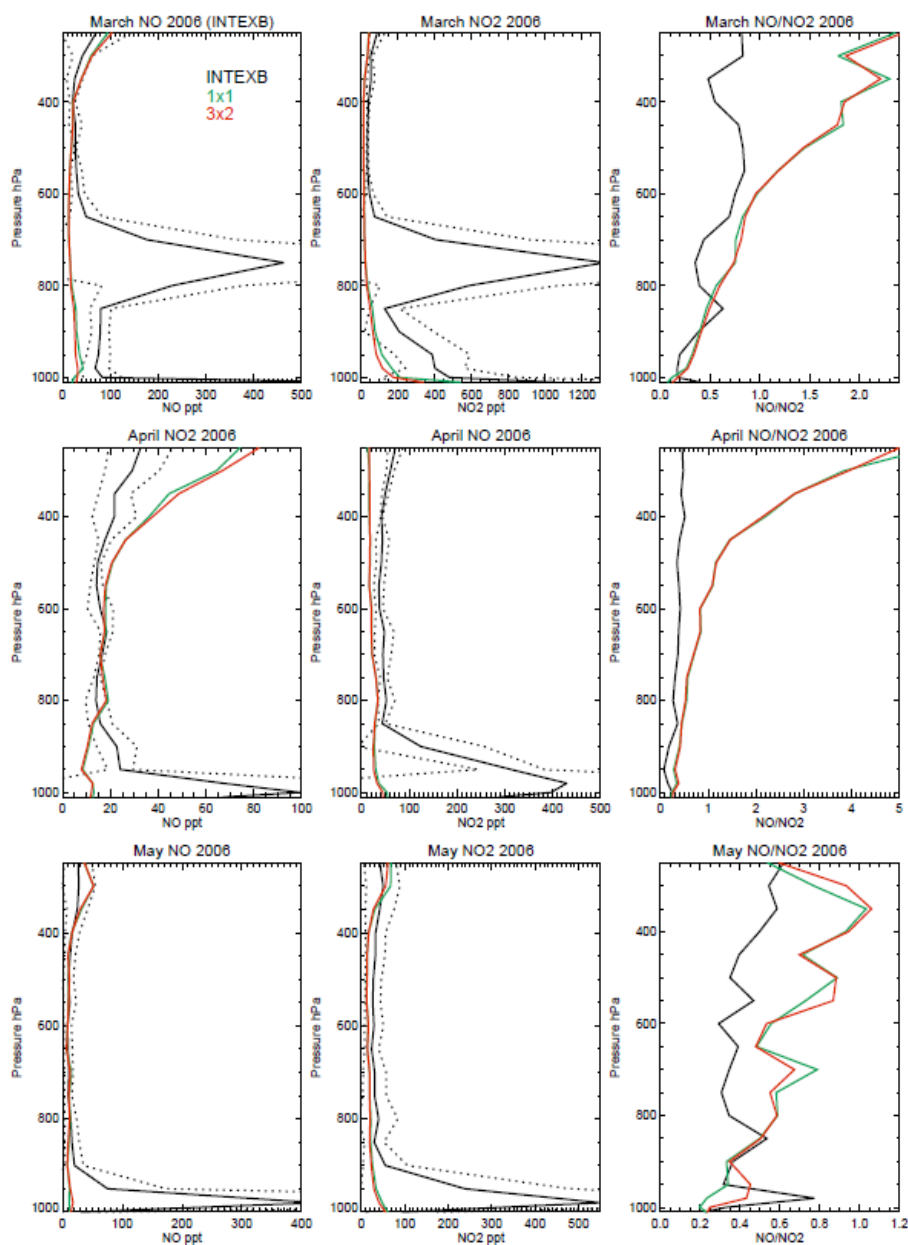


Figure 6: Monthly mean comparisons of NO (left), NO₂ (middle) and the resulting NO/NO₂ ratio from the INTEX-B measurements and TM5-MP simulations. The dotted line represents the 1- σ deviation in the mean of the measurements. For details of the locations for each month the reader is referred to Singh et al. (2009).



34

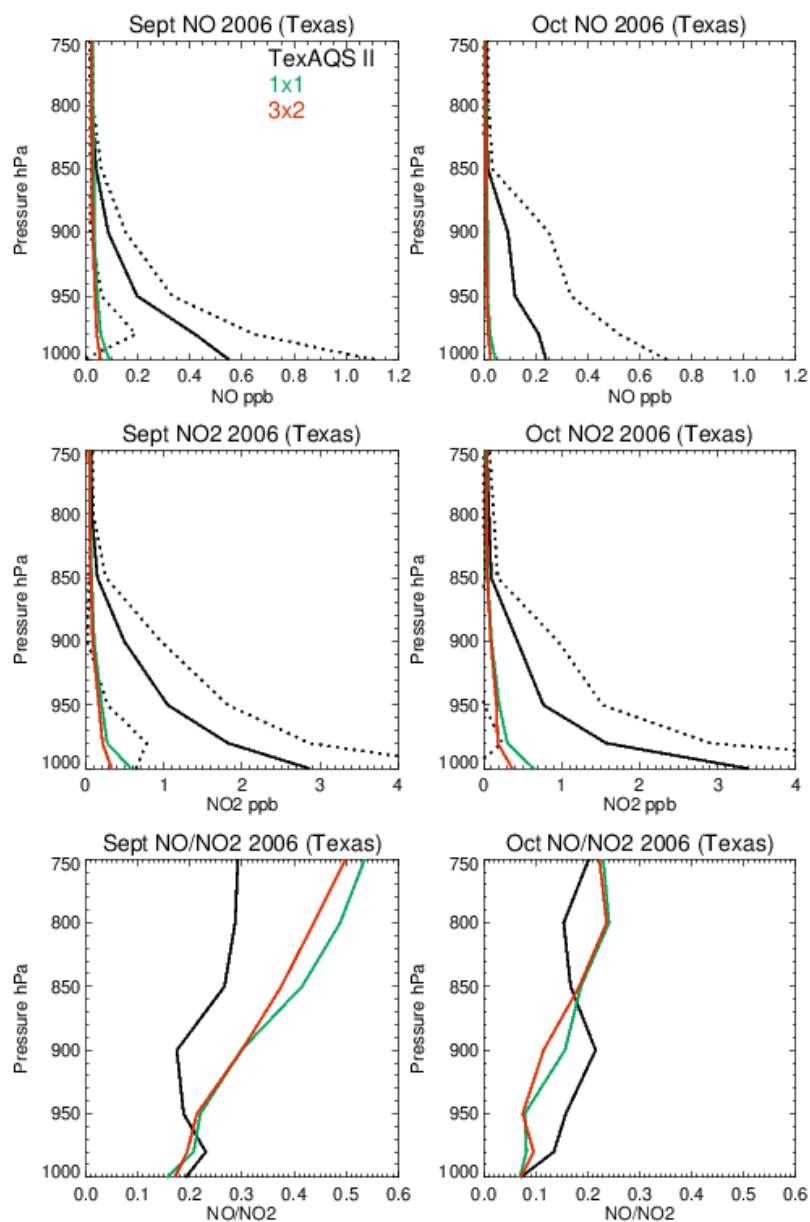


Figure 7: Monthly mean comparisons of NO (left), NO₂ (middle) and the resulting NO/NO₂ ratio from the TexAQSII campaign during September 2006 and TM5-MP simulations. The dotted line represents the 1-σ deviation in the mean of the measurements. For details of the locations for each month the reader is referred to Parrish et al. (2009).



35

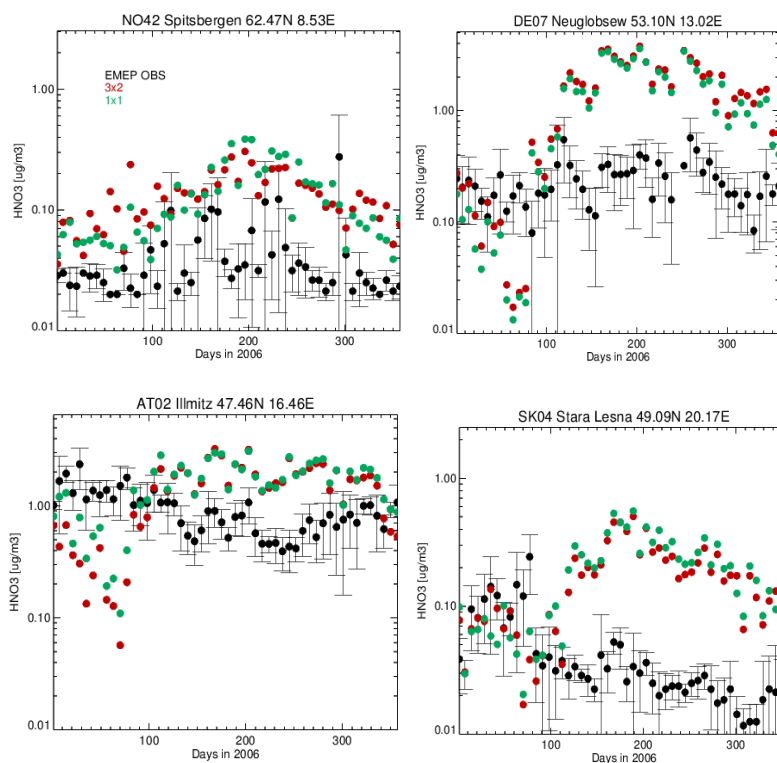


Figure 8: Comparison of weekly HNO_3 concentrations ($\mu\text{g m}^{-3}$) from both $3^\circ \times 2^\circ$ and $1^\circ \times 1^\circ$ simulations at 4 selected EMEP sites for 2006. The $1-\sigma$ deviation in the weekly observations are shown as error bars. The selected sites shown are in Norway (top left), Germany (top right), Austria (bottom left) and Slovakia (bottom right).



36

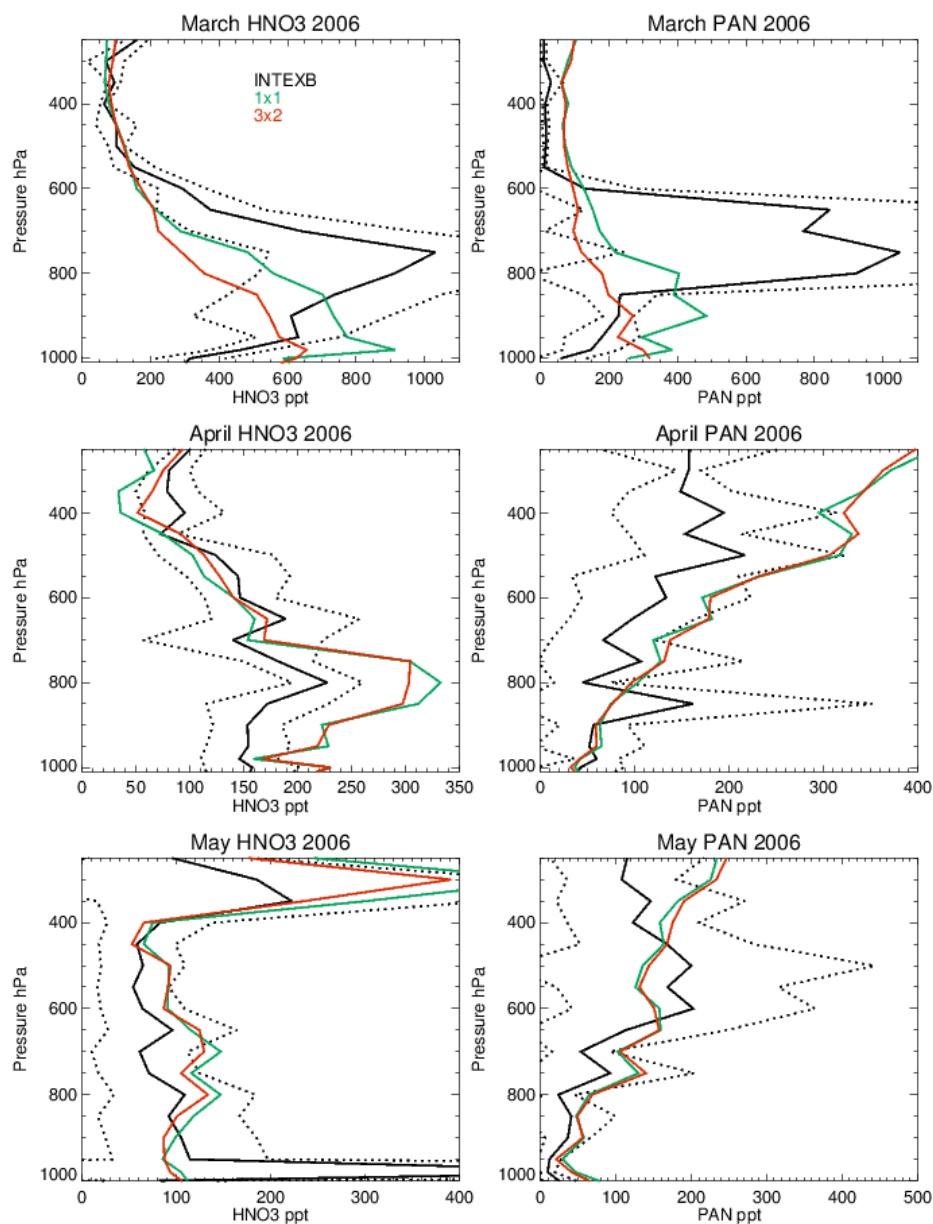


Figure 9: Monthly mean comparisons of HNO_3 (left) and PAN (right) from the INTEx-B measurements and TM5-MP simulations. The dotted line represents the 1- σ deviation in the mean of the measurements. For details of the locations for each month the reader is referred to Singh et al. (2009).

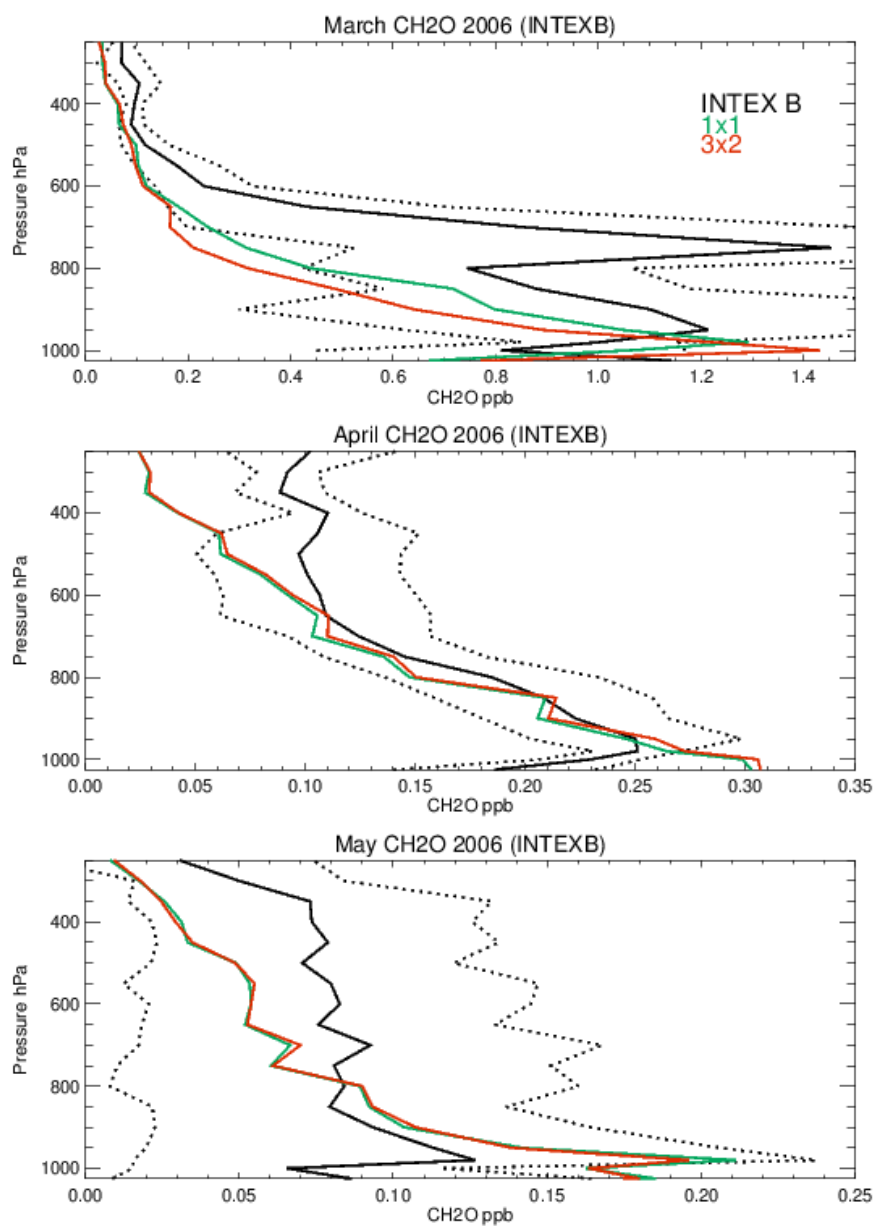


Figure 10: Comparisons of the vertical distribution of CH_2O from both $3^\circ \times 2^\circ$ and $1^\circ \times 1^\circ$ simulations against measurements made as part of the INTEX B during 2006. The dotted line represents the $1\text{-}\sigma$ deviation in the mean of the measurements. For details on the exact location of the flights the reader is referred to Parrish et al. (2009).

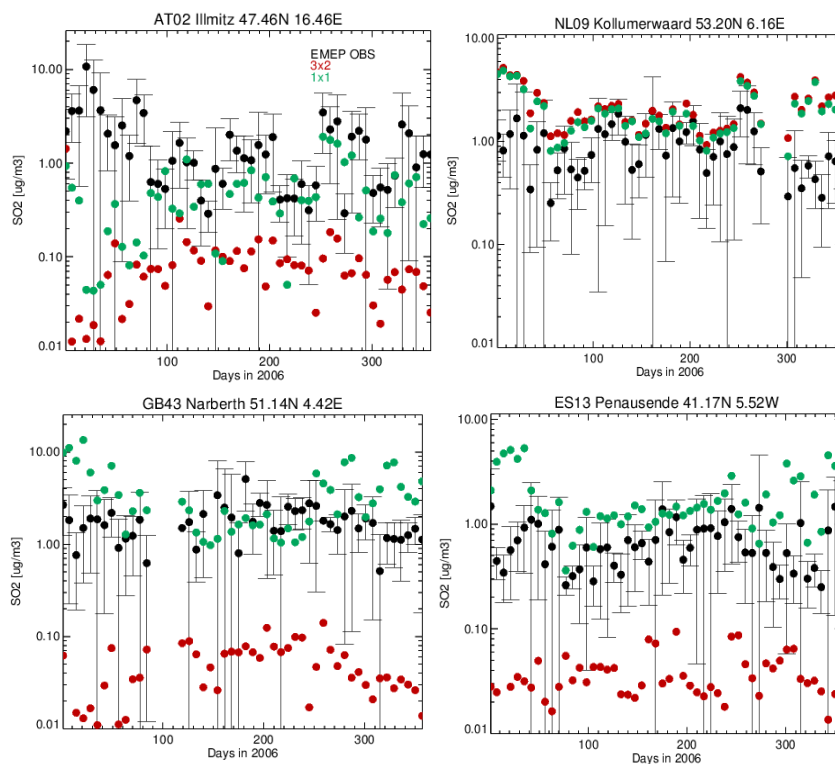


Figure 11: Comparison of hourly SO_2 concentrations ($\mu\text{g m}^{-3}$) at 13:00 from both the $3^\circ \times 2^\circ$ and $1^\circ \times 1^\circ$ simulations at 4 selected EMEP sites for 2006. The selected sites shown are in Austria (top left), the Netherlands (top right), Great Britain (bottom left) and Spain (bottom right).



862

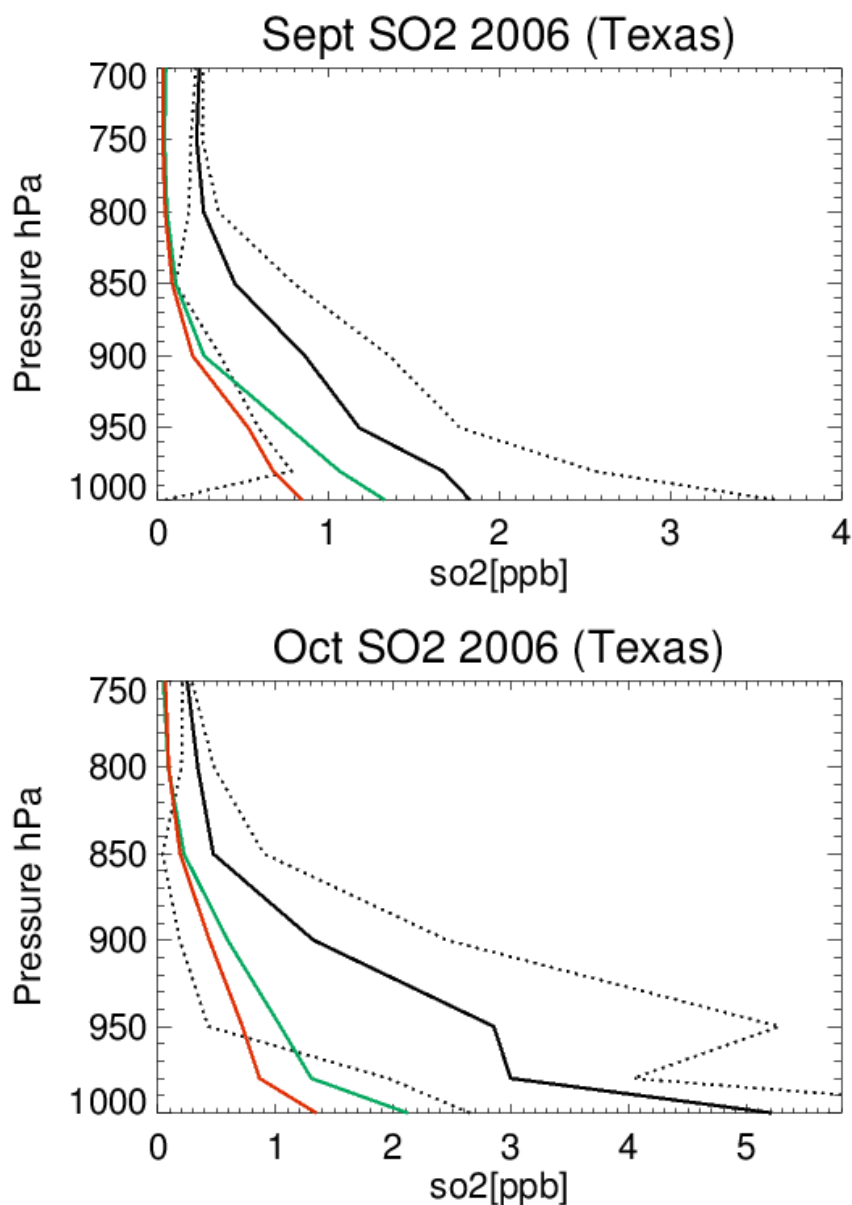


Figure 12: Comparisons of the monthly tropospheric SO₂ profile assembled from data taken during September and October 2006 as part of the Texas-AQS II. The 1- σ deviation from the measurements is shown as the dotted line for each of the days. For details of the flight paths the reader is referred to the details given in Parrish et al. (2009).

863
 864
 865
 866
 867
 868
 869



870 **References**

- 871 Aan de Brugh, J. M. J., Schaap, M., Vignati, E., Dentener, F., Kahnert, M., Sofiev, M., Huijnen, V., and Krol,
872 M. C.: The European aerosol budget in 2006, *Atms. Phys. Chem.*, 11, 1117-1139, doi:10.5194/acp-11-1117-
873 2011, 2011.
- 874 Aas, W., Hjellbrekke, A.-G., Schaug, J., and Solberg, S.: Data quality 1999, quality assurance and field
875 comparisons, Kjeller, Norwegian Institute for Air Research, EMEP/CCC Report 6/2001, 2001.
- 876 Abbatt, J. P. D., Lee, A. K. Y., and Thornton, J. A.: quantifying trace gas uptake to tropospheric aerosol: recent
877 advances and remaining challenges, *Chem. Soc. Rev.*, 41, 6555–6581, doi:10.1039/c2cs35052a, 2012.
- 878 Alonza Gray, B., Wang, Y., Gu, D., Bandy, A., Mauldin, L., Clarke, A., Alexander, B., and Davis, D. D.:
879 Sources, transport, and sinks of SO₂ over the equatorial Pacific during the Pacific Atmospheric Sulfur
880 Experiment, *J. Atmos. Chem.*, 68, 27-53, doi: 10.1007/s10874-010-9177-7, 2011.
- 881 Atkinson, R., Baulch, D. L., Cox, R. A., Crowley, J. N., Hampson, R. F., Hynes, R. G., Jenkin, M. E., Rossi, M.
882 J., and Tore, J., Evaluated kinetic and photochemical data for atmospheric chemistry: Volume I –gas phase
883 reactions of O_x, HO_x, NO_x and SO_x species, *Atmos. Chem. Phys.*, 4, 1461-1738, 2004.
- 884 Atkinson, R., Baulch, D. L., Cox, R. A., Crowley, J. N., Hampson, R. F., Hynes, R. G., Jenkin, M. E., Rossi, M.
885 J., and Tore, J., Evaluated kinetic and photochemical data for atmospheric chemistry: Volume II –gas phase
886 reactions of organic species, *Atmos. Chem. Phys.*, 6, 3625-4055, 2006.
- 887 Bândă, N., Krol, M., van Noije, T., van Weele, M., Williams J. E., Le Sager, P., Niemeier, U., Thomason, L.
888 and Röckmann, T.: The effect of stratospheric sulfur from Mount Pinatubo on tropospheric oxidizing capacity
889 and methane, *J. Geophys. Res. Atmos.*, 120, doi:10.1002/2014JDO22137, 2015.
- 890 Boersma, K. F., Jacob, D. J., Eskes, H. J., Pinder, R. W., Wang, J. and van der A, R. J.: Intercomparison of
891 SCIAMACHY and OMI tropospheric NO₂ columns: observing the diurnal evolution of chemistry and emissions
892 from space, *J. Geophys. Res.*, 2, 113, 1-14, doi:10.1029/2007JD008816, 2008.
- 893 Boersma, K. F., Eskes, H. J., Dirksen, R. J., van der A, R. J., Veefkind, J. P., Stammes, P., Huijnen, V.,
894 Kleipool, Q. L., Sneep, M., Claas, J., Leitao, J., Richter, A., Zhou, Y. and Brunner, D.: An improved
895 tropospheric NO₂ column retrieval algorithm for the Ozone Monitoring Instrument, *Atmos. Meas. Tech.*, 4,
896 1905-1928, 2011.
- 897 Bregman, B., Segers, A., Krol, M., Meijer, E., and van Velthoven, P.: On the use of mass-conserving wind fields
898 in chemistry-transport models, *Atmos. Chem. Phys.*, 3, 447–457, doi:10.5194/acp-3-447-2003, 2003.
- 899 Browne, E. C., Perring, A. E., Wooldridge, P. J., Apel, E., Hall, S. R., Huey, L. G., Mao, J., Spencer, K. M., St.
900 Clair, J. M., Weinheimer, A. J., Wisthaler, A., and Cohen, R. C.: Global and regional effects of the
901 photochemistry of CH₃ONO₂: evidence from ARCTAS, *Atmos. Chem. Phys.*, 11, 4209-4219, 2011.
- 902 Carslaw, D. C. and Beevers, S. D.: Estimations of road vehicle primary NO₂ exhaust emission fractions using
903 monitoring data in London, *Atmos. Environ.*, 39(1), 167-177, 2005.



- 904 De Smedt, I., Muller, J.-F., Stavrou, T., van der A., R., Eskes, H. and Van Roozendael, M.: Twelve years of
905 global observations of formaldehyde in the troposphere using GOME and SCIAMACHY sensors, *Atmos. Chem.*
906 *Phys.*, 8, 4947–4963, 2008.
- 907 Dee, D. P., Uppala, S. M., Simmons, A. J., Berrisford, P., Poli, P., Kobayashi, S., Andrae, U., Balmaseda, M. A.,
908 Balsamo, G., Bauer, P., Bechtold, P., Beljaars, A. C. M., van de Berg, L., Bidlot, J., Bormann, N., Delsol, C.,
909 Dragani, R., Fuentes, M., Geer, A. J., Haimberger, L., Healy, S. B., Hersbach, H., Hólm, E. V., Isaksen, I.,
910 Kållberg, P., Köhler, M., Matricardi, M., McNally, A. P., Monge-Sanz, B. M., Morcrette, J.-J., Park, B.-K.,
911 Peubey, C., de Rosnay, P., Tavolato, C., Thépaut, J.-N. and Vitart, F.: The ERA-Interim reanalysis:
912 configuration and performance of the data assimilation system, *Q. J. Royal Met. Soc.*, 137, 656, 553–597, 2011.
- 913 Dunlea, E. J., Herndon, S. C., Nelson, D. D., Volkamer, R. M., San Martini, F., Sheehy, P. M., Zahniser,
914 M. S., Shorter, J. H., Wormhoudt, J. C., Lamb, B. K., Allwine, E. J., Gaffney, J. S., Marley, N. A., Grutter, M.,
915 Marquez, C., Blanco, S., Cardenas, B., Retama, A., Ramos Villegas, C. R., Kolb, C. E., Molina, L. T., and
916 Molina, M. J.: Evaluation of nitrogen dioxide chemiluminescence monitors in a polluted urban environment,
917 *Atmos. Chem. Phys.*, 7, 2691–2704, 2007, <http://www.atmos-chem-phys.net/7/2691/2007/>
- 918 Dupuy, E., Urban, J., Ricaud, P., Le Flochmoën, E., Lautié, N., Murtagh, D., De La Noë, J., El Amraoui, L.,
919 Eriksson, P., Forkman, P., Frisk, U., Jégou, F., Jiménez, C. and Olberg, M.: Starto-mesospheric measurements of
920 carbon monoxide with the Odin Sub-Millimetre Radiometer: Retrieval and first results, *Geophys. Res. Letts.*, 31,
921 L20101, doi:10.1029/2004GL020558, 2004.
- 922 Emmons, L. K., Walters, S., Hess, P. G., Lamarque, J.-F., Pfister, G. G., Fillmore, D., Granier, C., Guenther, A.,
923 Kinnison, D., Laepple, T., Orlando, J., Tie, X., Tyndall, G., Wiedinmyer, C., Baughcum, S. L., and Kloster, S.:
924 Description and evaluation of the Model for Ozone and Related chemical Tracers, version 4 (MOZART-4),
925 *Geosci. Model Dev.*, 3, 43–67, doi: 10.5194/gmd-3-43-2010, 2010.
- 926 Evans, M. J. and Jacob, D. J.: Impact of new laboratory studies of N₂O₅ hydrolysis on global model budgets of
927 tropospheric nitrogen oxides, ozone and OH, *Geophys. Res. Letts.*, 32, doi:10.1029/2005GL022469, 2005.
- 928 Fortuin, J. P. F. and Kelder, H.: An ozone climatology based on ozonesonde and satellite measurements. *J.*
929 *Geophys. Res.*, 103, 31709–31734, 1998.
- 930 Gonçalves, M., Dabdub, D., Chang, W. L., Jorba, O. and Baldasano, J. M.: Impact of HONO sources on the
931 performance of mesoscale air quality models, *Atmos. Environ.*, 54, Pages 168–176,
932 doi:10.1016/j.atmosenv.2012.02.079, 2012.
- 933 Gonzi, S., Palmer, P. I., Barkley, M., De Smedt, I. and Roozendael, M. V.: Biomass burning emission estimates
934 inferred from satellite column measurements of HCHO: Sensitivity to co-emitted aerosol and injection height,
935 *Geophys. Res. Letts.*, 38, L14807, 2011.
- 936 Granier, C., Bessagnet, B., Bond, T., D’Angiola, A., Denier van der Gon, H., Frost, G. J., Heil, A., Kaiser, J. W.,
937 Kinne, S., Klimont, Z., Kloster, S.-F., Lamarque, J., Liousse, C., Masui, T., Meleux, F., Mieville, A., Ohara, T.,
938 Raut, J.-C., Riahi, K., Schultz, M. G., Smith, S. J., Thompson, A., van Aardenne, J., van der Werf, G. R., and
939 van Vuuren, D. P.: Evolution of anthropogenic and biomass burning emissions of air pollutants at global and



- 940 regional scales during the 1980–2010 period, *Climate Change*, 109, 163–190, doi: 10.1007/s10584-011-0154-
941 115, 2011.
- 942 Groöß, J.-U. and Russell III, J. M.: Technical note: A stratospheric climatology for O₃, H₂O, CH₄, NO_x, HCl and
943 HF derived from HALOE measurements, *Atmos. Chem. Phys.*, 5, 2797–2807, doi:10.5194/acp-5-2797-2005,
944 2005.
- 945 Hardacre, C., Wild, O. and Emberson, L.: An evaluation of ozone dry deposition in global scale chemistry
946 climate models, *Atms. Chem. Phys.*, 15, 6419–6436, doi:10.5194/acp-15-6419-2015, 2015.
- 947 Hauglustaine, D. A., Balkanski, Y. and Schulz, M.: A global model simulation of present and future nitrate
948 aerosols and their direct radiative forcing of climate, *Atms. Chem. Phys.*, 14, 11031–11063, doi:10.5194/acp-14-
949 11031-2014, 2014.
- 950 Heckel, A., Kim, S.-W., Frost, G. J., Richter, A., Trainer, M. and Burrows, J. P.: Influence of low spatial
951 resolution a priori data on tropospheric NO₂ satellite retrievals, *Atmos. Meas. Tech.*, 4, 1805–1820, 2011.
- 952 Huijnen, V., Williams, J., van Weele, M., van Noije, T., Krol, M., Dentener, F., Segers, A., Houweling, S.,
953 Peters, W., de Laat, J., Boersma, F., Bergamaschi, P., van Velthoven, P., Le Sager, P., Eskes, H., Alkemade, F.,
954 Scheele, R., Nédelec, P., and Pätz, H.-W., The global chemistry transport model TM5: description and
955 evaluation of the tropospheric chemistry version 3.0, *Geosci. Model Dev.*, 3, 445–473, 2010.
- 956 Huijnen, V., Williams, J. E., and Flemming, J.: Modeling global impacts of heterogeneous loss of HO₂ on cloud
957 droplets, ice particles and aerosols, *Atmos. Chem. Phys. Discuss.*, 14, 8575–8632, doi: 10.5194/acpd-14-8575-
958 2014, 2014.
- 959 Jacob, D. J., Prather, M. J., Rasch, P. J., Shia, R. L., Balkanski, Y. J., Beagley, S. R., Bergmann, D. J.,
960 Blackshear, W. T., Brown, M., Chiba, M., Chipperfield, M. P., de Grandpré, J., Dignon, J. E., Feichter, J.,
961 Genthon, C., W. L. Grose, W. L., Kasibhatla, P. S., Köhler, I., Kritz, M. A., Law, K., Penner, J. E., Ramonet,
962 M., Reeves, C. E., Rotman, D. A., Stockwell, D. Z., Van Velthoven, P. F. J., Verver, G., Wild, O., Yang, H and
963 Zimmermann, P.: Evaluation and intercomparison of global atmospheric transport models using ²²²Rn and other
964 short-lived tracers, *J. Geophys. Res.*, 102(D5), 5953–5970, doi:10.1029/96JD02955, 1997.
- 965 Jacob, J. D.: Heterogeneous chemistry and tropospheric ozone, *Atmos. Environ.*, 34, 2131–2159, 2000.
- 966 Jégou, F., Urban, J., de La Noë, J., Ricaud, P., Le Flochmoën, E., Murtagh, D. P., Eriksson, P., Jones, A.,
967 Petelina, S., Llewellyn, E. J., Lloyd, N. D., Haley, C., Lumpe, J., Randall, C., Bevilacqua, R. M., Catoire, V.,
968 Huret, N., Berthet, G., Renard, J. B., Strong, K., Davies, J., Mc Elroy, C. T., Goutail, F., and Pommereau, J. P.:
969 Technical Note: Validation of Odin/SMR limb observations of ozone, comparisons with OSIRIS, POAM III,
970 ground-based and balloon-borne instruments, *Atmos. Chem. Phys.*, 8, 3385–3409, doi:10.5194/acp-8-3385-
971 2008, 2008.
- 972 Kim, S.-W., McKeen, S. A., Frost, G. J., S.-H. Lee, S.-H., M. Trainer, M., Richter, A., Angevine, W. M., Atlas,
973 E., Bianco, L., Boersma, K. F., Brioude, J., Burrows, J. P., de Gouw, J., Fried, A., Gleason, J., Hilboll, A.,
974 Mellqvist, J., Peischl, J., Richter, D., Rivera, C., Ryerson, T., te Lintel Hekkert, S., Walega, J., Warneke,
975 C., Weibring, P., and Williams, E.: Evaluations of NO_x and highly reactive VOC emission inventories in Texas



- 976 and their implications for ozone plume simulations during the Texas Air Quality Study 2006, *Atmos. Chem.*
- 977 *Phys.*, 11, 11361–11386, doi:10.5194/acp-11-11361-2011, 2011.
- 978 Krol, M., Houweling, S., Bregman, B., van den Broek, M., Segers, A., van Velthoven, P., Peters, W., Dentener,
- 979 F., and Bergamaschi, P.: The two-way nested global chemistry-transport zoom model TM5: algorithm and
- 980 applications, *Atmos. Chem. Phys.*, 5, 417–432, doi:10.5194/acp-5-417-2005, 2005.
- 981 Lawrence, M. G. and Crutzen, P. J.: The impact of cloud particle gravitational settling on soluble trace gas
- 982 distributions, *Tellus*, 50B, 263–289, 1998.
- 983 Lee, C., Martin, R. V., van Donkelaar, A., Lee, H., Dickerson, R. R., Hains, J. C., Krotkov, N., Richter, A.,
- 984 Vinnikov, K. and Schwab, J. J.: SO₂ emissions and lifetimes: Estimates from inverse modeling using in situ and
- 985 global, space-based (SCIAMACHY and OMI) observations, *J. Geophys. Res.*, 116, D06304,
- 986 doi:10.1029/2010JD014758, 2011.
- 987 Lelieveld, J., Peters, W., Dentener, F. J., and Krol, M. C.: Stability of tropospheric hydroxyl chemistry, *J.*
- 988 *Geophys. Res.*, 107(D23), 4715, doi:10.1029/2002JD002272, 2002.
- 989 Lin, J. T., Martin, R. V., Boersma, K. F., Sneep, M., Stammes, P., Spurr, R., Wang, P., Van Roozendaal, M.,
- 990 Clémer, K., and Irie, H.: Retrieving tropospheric nitrogen dioxide from the Ozone Monitoring Instrument:
- 991 effects of aerosols, surface reflectance anisotropy, and vertical profile of nitrogen dioxide, *Atmos. Chem. Phys.*,
- 992 14, 1441–1461, doi:10.5194/acp-14-1441-2014, 2014.
- 993 Lee, C., Martin, R. V., van Donkelaar, A., Lee, H., Dickerson, R. R., Hains, J. C., Krotkov, N., Richter, A.,
- 994 Vinnikov, K. and Schwab, J. J.: SO₂ emissions and lifetimes: Estimates from inverse modeling using in situ and
- 995 global, space-based (SCIAMACHY and OMI) observations, *J. Geophys. Res.*, 116, D06304,
- 996 doi:10.1029/2010JD014758, 2011.
- 997 Marais, E. A., Jacob, D. J., Kurosu, T. P., Chance, K., Murphy, J. C., Reeves, C., Mills, G., Casadio, S., D. B.
- 998 Millet, D. B., Barkley, M. P., Paulot, F., and Mao, J.: Isoprene emissions in Africa inferred from OMI
- 999 observations of formaldehyde columns, *Atms. Chem. Phys.*, 12, 6219–6235, doi:10.5194/acp-12p6219-2012,
- 1000 2012.
- 1001 Martin, G. M., Johnson, D. W., and Spice, A.: The measurement and parameterization of effective radius of
- 1002 droplets in warm stratocumulus clouds, *J. Atmos. Sci.*, 51, 1823–1842, 1994.
- 1003 Meijer, E. W., van Velthoven, P. F. J., Brunner, D. W., Huntrieser, H., and Kelder, H.: Improvement and
- 1004 evaluation of the parameterisation of nitrogen oxide production by lightning, *Phys. Chem. Earth*, 26, 557–583,
- 1005 2001.
- 1006 Meloen, J., Siegmund, P., van Velthoven, P., Kelder, H., Sprenger, M., Wernli, H., Kentarchos, A., Roelofs, G.,
- 1007 Feichter, J., Land, C., Forster, C., James, P., Stohl, A., Collins, W., and Cristofanelli, P.: Stratosphere-
- 1008 troposphere exchange: A model and method intercomparison, *J. Geophys. Res.*, 108(D12), 8256,
- 1009 doi:1029/2002JD002274, 2002.
- 1010 Möllner, A. K., Valluvadasan, S., Feng, L., Sprague, M. K., Okumura, M., Milligan, D. B., Bloss, W.J., Sander,
- 1011 S. P., Martien, P. T., Harley, R. A.,



- 1012 Olsen, S. C., McLinden, C. A., and Prather, M. J.: Stratospheric N₂O–NO_y system: Testing uncertainties in a
1013 three-dimensional framework, *J. Geophys. Res.*, 106, 28771–28784, 2001.
- 1014 Olszyna, K. J., Bailey, E. M., Simonaitis, R. and Meagher, J. F.: O₃ and NO_y relationships at a rural site, 99(D7),
1015 14557–14563, doi:10.1029/94JD00739, 1994.
- 1016 Palmer, P. I., Abbot, D. S., Fu, T.-M., Jacob, D. J., Chance, K., Kurosu, P., Guenther, A., Wiedinmyer, C.,
1017 Stanton, J. C., Pilling, M. J., Pressley, S. N., Lamb, B. and Sumner, A. L.: Quantifying the seasonal and
1018 interannual variability of North American isoprene emissions using satellite observations of the formaldehyde
1019 column, *J. Geophys. Res.*, 111, D12315, doi:10.1029/2005JD006689, 2006.
- 1020 Parrish, D. D., Allen, D. T., Bates, T. S., Estes, M., Fehsenfeld, F. C., Feingold, G., Ferrare, R., Hardesty, R. M.,
1021 Meagher, J. F., Nielsen-Gammon, J. W., Pierce, R. B., Ryerson, T. B., Seinfeld, J. H. and Williams, E. J.:
1022 Overview of the Second Texas Air Quality Study (TexAQS II) and the Gulf of Mexico Atmospheric
1023 Composition and Climate study (GoMACCS), *J. Geophys. Res.*, 114 (D00F13), doi: 10.1029/2009JD011842,
1024 2009.
- 1025 Phillips, G. J., Makkonen, U., Schuster, G., Sobanski, N., Hakola, H. and Crowley, J. N.: The detection of
1026 nocturnal N₂O₅ as HNO₃ by alkali- and aqueous-denuder techniques, *Atmos. Meas. Tech.*, 6, 231–237,
1027 doi:10.5194/amt-6-231-2013, 2013.
- 1028 Pope, R. J., Chipperfield, M. P., Savage, N. H., Ordóñez, C., Neal, L.S., Lee, L.A., Dhomse, S. S., Richards, N.
1029 A. D. and Keslake, T. D.: Evaluation of a regional air quality model using satellite column NO₂: treatment of
1030 observation errors and model boundary conditions and emissions, *Atmos. Chem. Phys.*, 15, 5611–5626,
1031 doi:10.5194/acp-15-5611-2015, 2015
- 1032 Russell, A. R., Perring, A. E., Valin, L. C., Bucse, E. J., Browne, E. C., Wooldridge, P. J. and Cohen, R. C.: A
1033 high spatial resolution retrieval of NO₂ column densities from OMI: method and evaluation, *Atmos. Chem.*
1034 *Phys.*, 11, 8543–8554, doi:10.5194/acp-11-8543-2011, 2011.
- 1035 Schery, S. D.: Progress on Global Rn²²² Flux Maps and Recommendations for Future Research, in: 1st
1036 International Expert Meeting on Sources and Measurements of Natural Radionuclides Applied to Climate and
1037 Air Quality Studies (Gif-sur-Yvette, France, June 2003), edited by: Barrie, L. A. and Lee, H. N., WMO TD
1038 1201, Gif-sur-Yvette, France, 43–47, 2004.
- 1039 Schwartz, S. E.: Mass-transport considerations pertinent to aqueous-phase reactions of gases in liquid-water
1040 clouds, in: *Chemistry of Multiphase Atmospheric Systems*, edited by: Jaechske, W., Springer, Heidelberg, 415–
1041 471, 1986.
- 1042 Seltzer, K. M., Vizuete, W. and Henderson, B. H.: Evaluation of updated nitric acid chemistry on ozone
1043 precursors and radiative effects, *Atmos. Chem. Phys. Discuss.*, 15, 3219–3255, 2015.
- 1044 Shettle, E. P. and Fenn, R. W.: Models for the aerosols of the lower atmosphere and the effects of the humidity
1045 variations on their optical properties, *Environ. Res. Paper*, 676, AFGL-TR-79-0114, 91 pp, 1979.



- 1046 Sindelarova, K., Granier, C., Bouarar, I., Guenther, A., Tilmes, S., Stavrakou, T., Muller, J.-F., Kuhn, U.,
1047 Stefani, P. and Knorr, W.: Global dataset of biogenic VOC emissions calculated by the MEGAN model over the
1048 last 30 years, *Atmos. Phys. Chem.*, 14, 9317–9341, doi:10.5194/acp-14-9317-2014, 2014.
- 1049 Singh, H. B., Brune, W. H., Crawford, J. H., et al.: Chemistry and transport of pollution over the Gulf of Mexico
1050 and the Pacific: spring 2006 INTEX-B campaign overview and first results, *Atmos. Chem. Phys.*, 9, 2301–2318,
1051 doi:10.5194/acp-9-2301-2009, 2009.
- 1052 Stavrakou, T., Müller, J.-F., De Smedt, I., Van Roozendaal, M., van der Werf, G. R., Giglio, L., and Guenther,
1053 A.: Global emissions of non-methane hydrocarbons deduced from SCIAMACHY formaldehyde columns
1054 through 2003–2006, *Atms. Chem. Phys.*, 9, 3663–3679, 2009.
- 1055 Steinbacher, M., Zellweger, C., Schwarzenbach, B., Bugmann, S., Buchmann, B., Ordóñez, C., Prevot, A. S. H.,
1056 and Hueglin, C.: Nitrogen oxides measurements at rural sites in Switzerland: bias of conventional measurement
1057 techniques, *J. Geophys. Res.*, 112, D11307, doi:10.1029/2006JD007971, 2007.
- 1058 Stevenson, D. S., Dentener, F. J., Schultz, M. G., Ellingsen, K., van Noije, T. P. C., Wild, O., Zeng, G., Amann,
1059 M., Atherton, M., Bell, N., Bergmann, D. J., Bey, I., Bulter, T., Cofala, J., Collins, W. J., Derwent, R. G.,
1060 Doherty, R. M., Drevet, J., Eskes, H. J., Fiore, A. M., Gauss, M., Hauglustaine, D. A., Horowitz, L. W., Isaksen,
1061 I. S. A., Krol, M. C., Lamarque, J.-F., Lawrence, M. G., Montanaro, V., Müller, J. F., Pitari, G., Prather, M. J.,
1062 Pyle, J. A., Rast, S., Rodriguez, J. M., Sanderson, M. G., Savage, N. H., Shindell, D. T., Strahan, S. E., Sudo, K.,
1063 and Szopa, S.: Multimodel ensemble simulations of present-day and near future tropospheric ozone, *J. Geophys.*
1064 *Res.*, 111, D08301, doi: 10.1029/2005JD006338, 2006.
- 1065 Sutton, R. T., Dong, B. and Gregory, J. M.: Land/sea warming ratio in response to climate change: IPCC AR4
1066 model results and comparison with observations, *Geophys. Res. Letts.*, 34(2), 10.1029/2006GL028164, 2007.
- 1067 Tang, Q., Prather, M. J. and Hsu, J.: Stratosphere-troposphere exchange ozone flux related to deep convection,
1068 *Geophys. Res. Letts.*, 38, L03806, doi:10.1029/2010GL046039, 2011.
- 1069 Thouret, V., Marenco, A., Logan, J. A., Nédélec, P., and Grouhel, C.: Comparisons of ozone measurements from
1070 the MOZAIC airborne program and the ozone sounding network at eight locations, *J. Geophys. Res.*, 103,
1071 25695–25720, 1998.
- 1072 Tiedtke, M.: A comprehensive mass flux scheme for cumulus parameterization in large-scale models, *Mon.*
1073 *Weather. Rev.*, 117(8), 1779–1800, 1989.
- 1074 Tørseth, K., Aas, W., Breivik, K., Fjaeraa, A. M., Fiebig, M., Hjellbrekke, A. G., Lund-Myrhe, C., Solberg, S.
1075 and Yttri, K. E.: Introduction to the European Monitoring and Evaluation Programme (EMEP) and observed
1076 atmospheric composition change during 1972–2009, *Atmospheric Chemistry and Physics*, 12, 5447–5481, 2012.
- 1077 Urban, J., Pommier, M., Murtagh, D. P., Santee, M. L., and Orsolini, Y. J.: Nitric acid in the stratosphere based
1078 on Odin observations from 2001 to 2009 – Part I: A global climatology, *Atmos. Chem. Phys.*, 9, 7031–7044,
1079 doi:10.5194/acp-9-7031-2009, 2009.



- 1080 Valks, P., Pinardi, G., Richter, A., Lambert, J.-C., Hao, N., Loyola, D., Van Roozendaal, M., and Emmadi, S.:
1081 Operational total and tropospheric NO₂ column retrieval for GOME-2, *Atmos. Meas. Tech.*, 4, 1491-1514,
1082 doi:10.5194/amt-4-1491-2011, 2011.
- 1083 van Geffen, J.H.G.M., Boersma, K. F., Eskes, H. J., Maasakkers J. D. and Veefkind, J. P., TROPOMI
1084 Algorithm Theoretical Basis Document (ATBD) tropospheric and total NO₂, S5P-KNMI-L2-0005-RP, 56pp,
1085 2016.
- 1086 van der A, R. J., Allaart, M. A. F., and Eskes, H. J.: Multi sensor reanalysis of total ozone, *Atmos. Chem. Phys.*
1087 *Discuss.*, 10, 11401-11448, doi: 10.5194/acpd-10-11401-2010, 2010.
- 1088 van der Werf, G. R., Randerson, J. T., Giglio, L., Collatz, G. J., Mu, M., Kasibhatla, P. S., Morton, D. C.,
1089 DeFries, R. S., Jin, Y., and van Leeuwen, T. T.: Global fire emissions and the contribution of deforestation,
1090 savanna, forest, agriculture, and peat fires (1997–2009) *Atmos. Chem. Phys.*, 10, 11707–11735, 2010,
1091 <http://www.atmos-chem-phys.net/10/11707/2010/>.
- 1092 Veefkind, J.P., Aben, I., McMullan, K., Förster, H., de Vries, J., Otter, G., Claas, J., Eskes, H. J., de Haan, J. F.,
1093 Kleipool, Q., van Weele, M., Hasekamp, O., Hoogeveen, R., Landgraf, J., Snel, R., Tol, P., Ingmann, P., Voors,
1094 R., Kruizinga, B., Vink, R., Visser, H. and Levelt, P. F.: TROPOMI on the ESA Sentinel-5 Precursor: A GMES
1095 mission for global observations of the atmospheric composition for climate, air quality and ozone layer
1096 applications, *Remote. Sens. Environ.*, 120, 70-83, doi:10.1016/j.rse.2011.09.027, 2012.
- 1097 Verstraeten, W. V., Neu, J. L., Williams, J. E., Bowman, K. W. and Worden, J. R.: Rapid increases in
1098 tropospheric ozone production and export from China, *Nature Geosci.*, 8, 690-695, doi: 10.1038/ngeo2493,
1099 2015.
- 1100 Vinken, G. C. M., Boersma, K. F., Jacob, D.J. and Meijer, E. W.: Accounting for non-linear chemistry of ship
1101 plumes in the GEOS-Chem global chemistry transport model, *Atms. Chem. Phys.*, 11, *Atmos. Chem. Phys.*,
1102 11707-11722, doi:10.5194/acp-11-11707-2011, 2011.
- 1103 Vinken, G. C. M., Boersma, K. F., Maasakkers, J. D., Adon, M. and Martin, R. V.: Worldwide biogenic soil
1104 NO_x emissions inferred from OMI NO₂ observations, *Atmos. Chem. Phys.*, 14, doi:10.5194/acp-14-10363-2014,
1105 10363–10381, 2014.
- 1106 Von Kuhlmann, R. and Lawrence, M. G.: The impact of ice uptake of nitric acid on atmospheric chemistry,
1107 *Atms. Chem. Phys.*, 6, 225-235, 2006.
- 1108 Wild, O. and Prather, M. J.: Global tropospheric ozone modeling: Quantifying errors due to grid resolution, *J.*
1109 *Geophys. Res.*, 111, D11305, doi:10.1029/2005JD006605, 2006.
- 1110 Williams, J. E., Strunk, A., Huijnen, V. and van Weele, M.: The application of the Modified Band Approach for
1111 the calculation of on-line photodissociation rate constants in TM5: implications for oxidative capacity, *Geosci.*
1112 *Model Dev.*, 5, 15-35, doi:10.5194/gmd-5-15-2012,2012.
- 1113 Williams, J. E., van Velthoven, P. F. J., and Brenninkmeijer, C. A. M.: Quantifying the uncertainty in simulating
1114 global tropospheric composition due to the variability in global emission estimates of Biogenic Volatile Organic
1115 Compounds, *Atmos. Chem. Phys.*, 13, 2857–2891, doi: 10.5194/acp-13-2857-2013, 2013.



- 1116 Williams, J. E., Le Bras, G., Kukai, A., Ziereis, H., and Brenninkmeijer, C. A. M.: The impact of the chemical
1117 production of methyl nitrate from the $\text{NO} + \text{CH}_3\text{O}_2$ reaction on the global distribution of alkyl nitrates, nitrogen
1118 oxides and tropospheric ozone: a global modeling study, *Atmos. Chem. Phys.*, 14, 2363-2382, 2014.
- 1119 Worden, J., Liu, X., Bowman, K., Chance, K., Beer, R., Eldering, A., Gunson, M. and Worden, H., Improved
1120 tropospheric ozone profile retrievals using OMI and TES radiances, *Geophys. Res. Lett.*, 34, L01809,
1121 doi:10.1029/2006GL027806, 2007.
- 1122 Yamaji, K., Ikeda, K., Irie, H., Kurokawa, J. and Ohara, T.: Influence of model grid resolution on NO_2 vertical
1123 column densities over East Asia, *J. Air. Waste Manage. Assoc.*, 64(4), 436-444, 2014.
- 1124 Yarwood, G., Rao, S., Yocke, M., and Whitten, G.: Updates to the carbon bond chemical mechanism: CB05,
1125 Final report to the US EPA, EPA Report Number: RT-0400675, available at: www.camx.com (last access: 15
1126 January 2014), 2005.
- 1127 Zeng, G., Williams, J. E., Fisher, J.A., Emmons, L. K., Jones, N. B., Morgenstern, O., Robinson, J., Smale, D.,
1128 Paton-Walsh, C. and Griffith, D. W. T.: Multi-model simulation of CO and HCHO in the Southern Hemisphere:
1129 comparison with observations and impact of biogenic emissions, *Atmos. Chem. Phys.*, 15, 7217-7245,
1130 doi:10.5194/acp-15-7217-2015, 2015.
- 1131 Zdunkowski, W. G., Welsch, R. M., and Kord, G. J.: An investigation of the structure of typical 2-stream
1132 methods for the calculation of solar fluxes and heating rates in clouds, *Contrib. Atmos. Phys.*, 53, 215-238, 1980.
- 1133 Zhou, Y., Brunner, D., Hueglin, C., Henne, S., and Staehelin, J.: Changes in OMI tropospheric NO_2 columns
1134 over Europe from 2004 to 2009 and the influence of meteorological variability. *Atmos Environ*, 46, 482-495,
1135 2012.
- 1136 Zyrichidou, I., Koukouli, M. E., Balis, D., Markakis, K., Poupkou, A., Katragkou, E., Kioutsoukakis, I., Melas,
1137 D., Boersma, K. F. and van Roozendaal, M.: Identification of surface NO_x emission sources on a regional scale
1138 using OMI NO_2 , *Atmos. Environ.*, 101, 82-93, 2015.